PHYSICAL REVIEW D **84,** 044024 (2011)

Stellar dynamics of extreme-mass-ratio inspirals

David Merritt,[1,*] Tal Alexander,[2,†] Seppo Mikkola,[3,‡] and Clifford M. Will[4,§]

[1]*Department of Physics and Center for Computational Relativity and Gravitation, Rochester Institute of Technology, Rochester, New York 14623, USA*

[2]*Faculty of Physics, Weizmann Institute of Science, POB 26, Rehovot, Israel*

[3]*Tuorla Observatory, University of Turku, Väisäläntie 20, Piikkiö, Finland*

[4]*McDonnell Center for the Space Sciences, Department of Physics, Washington University, St. Louis, Missouri 63130, USA*

(Received 15 February 2011; published 5 August 2011)

Inspiral of compact stellar remnants into massive black holes (MBHs) is accompanied by the emission of gravitational waves at frequencies that are potentially detectable by space-based interferometers. Event rates computed from statistical (Fokker-Planck, Monte-Carlo) approaches span a wide range due to uncertaintities about the rate coefficients. Here we present results from direct integration of the post-Newtonian N-body equations of motion describing dense clusters of compact stars around Schwarzschild MBHs. These simulations embody an essentially exact (at the post-Newtonian level) treatment of the interplay between stellar dynamical relaxation, relativistic precession, and gravitational-wave energy loss. The rate of capture of stars by the MBH is found to be greatly reduced by relativistic precession, which limits the ability of torques from the stellar potential to change orbital angular momenta. Penetration of this ''Schwarzschild barrier'' does occasionally occur, resulting in capture of stars onto orbits that gradually inspiral due to gravitational wave emission; we discuss two mechanisms for barrier penetration and find evidence for both in the simulations. We derive an approximate formula for the capture rate, which predicts that captures would be strongly disfavored from orbits with semi-major axes below a certain value; this prediction, as well as the predicted rate, are verified in the N-body integrations. We discuss the implications of our results for the detection of extreme-mass-ratio inspirals from galactic nuclei with a range of physical properties.

DOI: 10.1103/PhysRevD.84.044024 PACS numbers: 04.30.Db, 04.25.Nx, 04.80.Cc

I. INTRODUCTION

Compact stellar remnants—white dwarfs, neutron stars, and stellar-mass black holes (BHs)—can be captured by massive black holes (MBHs) at the centers of galaxies like the Milky Way, without suffering tidal disruption in the process. Such extreme-mass-ratio inspirals (EMRIs) are a potential source of low-frequency gravitational waves (GWs) for space-based GW interferometers [1–4]. Capture orbits for EMRIs can be very eccentric [5], displaying extreme versions of relativistic precession. Typical EMRIs will have low, instantaneous GW amplitudes, but signals can potentially be observed over $\gtrsim 10^5$ cycles as the compact objects gradually lose energy and spiral in, allowing the signal-to-noise ratio to be built up over time using matched filtering or other techniques [6–8]. Detailed information about the structure of spacetime is encoded in the GW signal, permitting strong-field tests of theories of gravity [9–11].

Predictions of the EMRI event rate span a wide range, from $\sim 10^{-9}$ yr^{-1} to $\sim 10^{-6}$ yr^{-1} per galaxy [12–17]. There are two basic sources of uncertainty. Only stars originating from tightly bound orbits, $\lesssim 10$ mpc (milliparsecs), can complete their inspiral without being scattered prematurely into the MBH or onto a wider orbit. But the number and distribution of stars and stellar remnants at these radii is essentially unconstrained, even in the Milky Way [18], and estimates of the event rate must therefore be based on extrapolation of the stellar distribution observed on much larger scales, or on theoretical models. In addition, the collisional dynamics of relativistic star clusters around MBHs are poorly understood.

This paper addresses the second source of uncertainty. We present results from long-term (10^6–10^7 yr), direct N-body simulations of clusters of compact stars around a MBH. Relativistic corrections to the equations of motion are included up to 2.5 post-Newtonian (PN) order [[19], hereafter Paper I]. These new simulations permit an essentially exact treatment of the interplay between stellar relaxation and GW emission, avoiding the approximations that must be made in statistical (Fokker-Planck, Monte-Carlo) treatments.

In such a statistical treatment of EMRI, Hopman and Alexander [16] have shown that the dynamical evolution leading to capture on an inspiral orbit is driven by ''resonant relaxation'' (RR)[20] due to the residual torques from the stellar background. They argued that relativistic, in-plane (Schwarzschild) precession plays a critical role in suppressing the stellar torques on eccentric orbits, thereby allowing the stars to follow quasi-periodic EMRI orbits,

*merritt@astro.rit.edu
†tal.alexander@weizmann.ac.il
‡mikkola@utu.fi
§cmw@wuphys.wustl.edu

rather than be strongly torqued into direct plunge orbits; the latter would produce non-periodic, broadband GW events that would be difficult to detect.

The simulations presented here reveal that the interplay between Newtonian torques and relativistic precession not only limits the effectiveness of stellar relaxation before it can drive stars into plunge orbits, but in fact creates a dynamical barrier, the "Schwarzschild barrier," which repels stars back to less eccentric orbits, thereby strongly mediating the EMRI rate. We develop a Hamiltonian model for the behavior of orbits near this barrier and use it to identify two modes by which stars can cross the barrier and become EMRIs. Evidence for both modes of barrier penetration are found in the N-body simulations.

In Sec. II, we summarize the computational techniques and the N-body initial conditions. In subsequent sections, we present results from integrations in which the PN terms are absent, or included only at the 2.5 PN (GW emission) level (Sec. IV); and in which all PN terms up to and including 2.5 PN are included (Sec. V). In Sec. V, we also present an extended discussion of orbital dynamics near the Schwarzschild barrier based on a Hamiltonian formulation. Section VI discusses the implications of our results for the rate of EMRI production in real galaxies and Sec. VII sums up.

We confine ourselves in this paper to non-rotating, i.e. Schwarzschild, MBHs. The consequences of spin will be discussed in a subsequent paper.

II. MODELS AND METHODS

The N-body systems considered here consist of a single massive particle, representing a massive black hole (MBH), and 50 lower-mass particles representing stellar remnants (referred to below, interchangeably, as either BHs or stars). Each BH particle had a mass 5×10^{-5} that of the MBH particle. If the latter is assigned a mass of

$$M_\bullet = 1 \times 10^6 \mathcal{M}_\odot, \tag{1}$$

the BH particles have masses of $m = 50\mathcal{M}_\odot$. This value is somewhat larger than the predicted masses of the BHs that form in stellar collapse, i.e. 10–20$\mathcal{M}_\odot$ [21]. The choice for $m/M_\bullet$ was motivated by the need to integrate the N-body systems for a time of order the two-body relaxation time, which scales as m^{-2} for a system of fixed N. Alternatively, if m is set to $10\mathcal{M}_\odot$, $M_\bullet = 2 \times 10^5 \mathcal{M}_\odot$; however, we note that the existence of MBHs with $M_\bullet \lesssim 10^6 \mathcal{M}_\odot$ is speculative.

Unless otherwise stated, we adopt $M_\bullet = 1.0 \times 10^6 \mathcal{M}_\odot$ below when quoting N-body results in physical units. In most cases, the dynamical theory used to interpret the N-body results will allow the event rates derived here to be scaled approximately to systems of different m and $M_\bullet$.

The initial orbital elements of the BH particles were selected randomly from the distribution

$$N(a, e^2) da de^2 = N_0 da de^2 \tag{2}$$

with a and e the semi-major axis and eccentricity of the Keplerian orbit about the MBH. Equation (2) corresponds to an isotropic (in velocity) distribution with configuration-space density

$$n(r) = n_0 \left(\frac{r}{r_0}\right)^{-2}. \tag{3}$$

This is roughly the expected radial dependence for a relaxed population around a MBH [17,22,23]. The initial distribution in semi-major axis was truncated above $a = a_2 = 10$ mpc and below $a = a_1 = 0.1$ mpc. Setting $N = 50$ and $m = 50\mathcal{M}_\odot$, the enclosed, distributed mass becomes

$$M_\star(<r) \approx 250\mathcal{M}_\odot \tilde{r}, \qquad \tilde{r} \lesssim 10, \tag{4}$$

where $\tilde{r}$ is the radius in units of mpc and the subscript "$\star$" indicates the distributed mass; i.e., the stars.

While the values of N and $m/M_\bullet$ were chosen primarily on the basis of computational convenience, the models adopted here are not necessarily poor representations of real galactic nuclei. Steady-state models of the center of the Milky Way galaxy [15,17] typically find that the distributed mass within ~100 mpc of the MBH is dominated by stellar BHs (as opposed to other types of stellar remnant, or stars) with $M_\star(r < 10 \text{ mpc}) \approx 10^3 \mathcal{M}_\odot$. Expressed in terms of the gravitational radius defined in Eq. (10), and assuming $\rho \propto r^{-2}$, a distributed mass of $10^3 \mathcal{M}_\odot$ within 10 mpc implies

$$M_\star(<r) \approx 200 \left(\frac{r}{10^4 r_g}\right). \tag{5}$$

By comparison, the scaling adopted above implies that for our models,

$$M_\star(<r) \approx 120 \left(\frac{r}{10^4 r_g}\right). \tag{6}$$

The N-body integrator is described elsewhere [24,25]; it includes PN accelerations of orders up to and including 2.5 (i.e. c^{-5}) in the interactions between the MBH and star particles. The algorithm was modified for the current study to allow merger of star particles with the MBH. The condition for a merger was an instantaneous separation [26]

$$r \le r_{\rm capt} = 8 r_g \tag{7}$$

or $\sim 4 \times 10^{-4}$ mpc if $M_\bullet = 10^6 \mathcal{M}_\odot$. The angular momentum and eccentricity of an orbit that just grazes the capture sphere are (in the Keplerian approximation)

$$L_m = \sqrt{2GM_\bullet r_{\rm capt}}, \qquad e_m = 1 - \frac{r_{\rm capt}}{a}. \tag{8}$$

For $a_1 \le a \le a_2$ and using the adopted value of $r_{\rm capt}$, the eccentricity of a capture orbit satisfies

$$4 \times 10^{-5} \lesssim 1 - e_m \lesssim 4 \times 10^{-3}. \quad (9)$$

The mass of a merged particle was added to that of the MBH in such a way that linear momentum was conserved.

An EMRI event was defined as any merger occurring from an orbit with semi-major axis, at the moment of capture, less than 0.01 mpc. Mergers occurring from orbits with larger a were recorded as ''plunges''.

While capture in its final stages would be driven by energy loss due to emission of GWs, as represented here by the 2.5 PN terms, the capture *rate* is determined primarily by dynamical interactions that take place far beyond r_g. In order to better understand the dynamical mechanisms leading to capture, three series of N-body integrations were carried out, incorporating different subsets of the full PN equations of motion defined in Paper I.

Series I: No PN terms were included. Stars were nevertheless allowed to merge with the MBH if they passed within $r_{\rm capt}$ (plunges).

Series II: The 2.5 PN terms were included. As a result, some stars (''EMRIs'') were captured onto orbits for which the time scale for GW energy loss is less than the time scale for scattering by other stars.

Series III: All PN terms (1 PN, 2 PN, 2.5 PN) were included.

In each series, at least eight different Monte Carlo realizations of the same initial conditions were integrated forward in time. Models from Series I and II were integrated for a time of 10^7 yr, based on the scalings adopted above. For models from Series III, inclusion of the additional PN terms caused the integrator to run more slowly, and most integrations were terminated after 2–3 Myr. Calculations were carried out on GRAVITYSIMULATOR, the 32-node cluster at RIT.

III. BASIC SCALES OF LENGTH AND TIME

Here we define length and time scales associated with an idealized model consisting of a central MBH and a smooth, spherical distribution of surrounding stars. Other time scales, associated with collisional (relaxation) processes, are defined below.

The length scale associated with the event horizon of the MBH is

$$r_g \equiv \frac{GM_\bullet}{c^2} \approx 4.80 \times 10^{-5}\ \text{mpc}, \quad (10)$$

where the numerical value assumes $M_\bullet = 1.0 \times 10^6 \mathcal{M}_\odot$.

Ignoring the contribution of the stellar BHs to the gravitational potential, the (Newtonian) orbital period of a test mass around the MBH is

$$P_r = \frac{2\pi a^{3/2}}{\sqrt{GM_\bullet}} \approx 2.96 \tilde{a}^{3/2}\ \text{yr}, \quad (11)$$

where $\tilde{a}$ is the test mass's semi-major axis in units of mpc; the second relation again assumes $M_\bullet = 1.0 \times 10^6 \mathcal{M}_\odot$.

Approximating the stellar BHs as a smooth mass distribution, $\rho(r) = mn(r)$ with $n(r)$ given by Eq. (3), their contribution to the gravitational potential is

$$\Phi_\star(r) = \frac{GM_0}{r_0} \ln\left(\frac{r}{r_0}\right) + \text{constant}, \quad (12)$$

where $M_\star(<r) = M_0(r/r_0)$; setting $r_0 = 1$ mpc gives $M_0 = 250\mathcal{M}_\odot$ in our models.

Deviation of the potential from that of a point mass induces a precession in the (fixed) plane of an orbiting star, the ''mass precession.'' Orbital perturbation theory [e.g. [27]] gives for the precession rate, in the limit $M_0 \ll M_\bullet$,

$$\frac{d\omega}{dt} \equiv \nu_{\rm M} \approx -\nu_r \frac{M_\star(r<a)}{M_\bullet} \frac{\sqrt{1-e^2}}{1+\sqrt{1-e^2}}, \quad (13)$$

where

$$\nu_r \equiv \frac{2\pi}{P_r} = (GM_\bullet)^{1/2} a^{-3/2} \approx (0.47\ \text{yr})^{-1} \tilde{a}^{-3/2} \quad (14)$$

is the radial frequency and e is the orbital eccentricity. Precession is retrograde, i.e. in the opposite sense to the orbital motion. For the adopted mass model [28],

$$t_{\rm M} \equiv \left|\frac{\pi}{\nu_{\rm M}}\right| \approx (1.18 \times 10^4\ \text{yr}) g(e) \tilde{a}^{1/2}, \quad (15a)$$

$$g(e) = \frac{1+\sqrt{1-e^2}}{2\sqrt{1-e^2}}. \quad (15b)$$

In the limit $e \to 1$, Eq. (13) predicts $\nu_{\rm M} \to 0$; i.e. radial orbits do not precess.

The PN accelerations also contribute to the in-plane precession. To lowest order, the Schwarzschild contribution is

$$\nu_{\rm GR} = \frac{3}{c^2} \frac{(GM_\bullet)^{3/2}}{(1-e^2)a^{5/2}} = \nu_r \frac{3r_g}{a(1-e^2)} \quad (16)$$

in the opposite (prograde) sense, and

$$t_{\rm GR} \equiv \left|\frac{\pi}{\nu_{\rm GR}}\right| \approx (1.02 \times 10^4\ \text{yr})(1-e^2)\tilde{a}^{5/2}. \quad (17)$$

While we defer a detailed treatment of spin effects to a subsequent paper, we note here that the Kerr contribution to the in-plane precession is smaller than (16) by a factor $\sim \chi(r_g/p)^{1/2}$, where χ is the dimensionless spin parameter of the MBH and $p = (1-e^2)a$ is the semi-latus rectum. Excepting very shortly before a merger, this factor would be much smaller than unity in our simulations.

IV. SERIES I AND II

As discussed in more detail below, including the relativistic terms in the N-body equations of motion resulted in much lower EMRI rates than expected based on Newtonian dynamics of a compact cluster around a

MBH. The essential element that differs between the relativistic and non-relativistic dynamics turns out to be the 1 PN precession of the periapse, Eq. (16). In order to quantify the magnitude of the differences, two sets of experiments were carried out in which some or all of the relativistic terms were omitted. Integrations from Series I were based on the Newtonian equations of motion. Series II included also the 2.5 PN terms, allowing capture of stars onto inspiral orbits via GW energy loss. In integrations from both Series I and Series II, the 1 PN (Schwarzschild) precession is absent.

A. Series I

Figure 1 shows, for one integration in Series I, the evolution of semi-major axis a and eccentricity e for each of the 50 stars, until a time of 2 Myr. Star-star gravitational scattering induces substantial changes in the orbital angular momenta over these time scales, while the energy (i.e. semi-major axis) remains nearly constant.

Whenever the periapse distance $r_p \equiv a(1-e)$ drops below $r_{\rm capt}$ the star is captured. Almost all such events are plunges since no GW energy loss occurs, and since essentially no stars have initial semi-major axes less than 0.01 mpc, the condition defined above for a capture to be classified as an EMRI. In the simulation shown in Fig. 1, 17 out of the 50 stars are captured by $t = 2$ Myr and 30 stars are captured by $t = 10$ Myr.

Figure 2 shows the time-averaged capture rate as a function of time, defined as the number of mergers occurring in time t divided by t. Events from each simulation in the series were summed and the result was divided by the number of simulations; in other words, the plotted rates refer to a cluster with $N(t=0) = 50$. The capture rate drops with time, since both the number of stars available to merge, and the number of stars acting as scatterers, decrease with time.

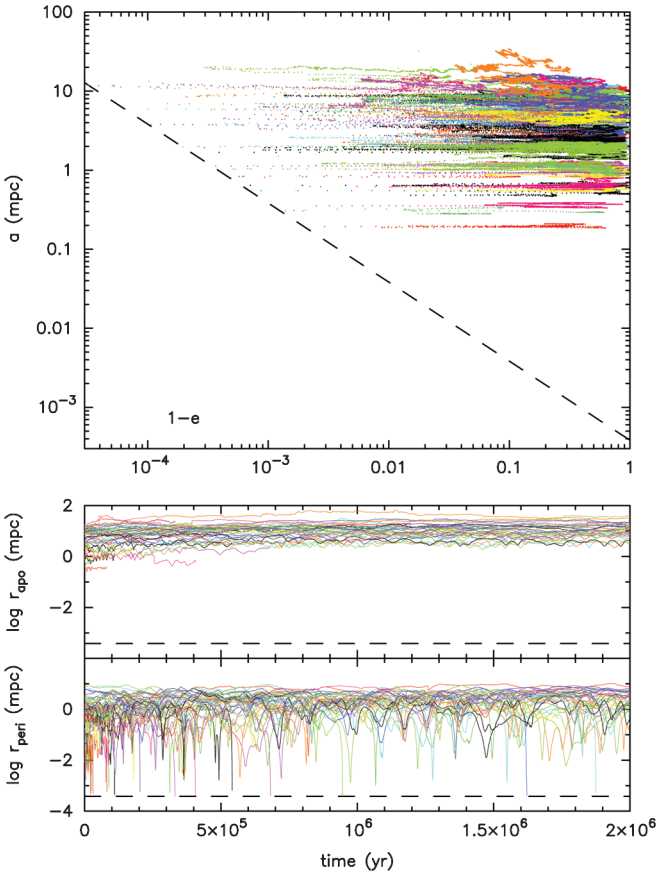

FIG. 1 (color). A simulation from Series I (Newtonian). a and e are the semi-major axis and eccentricity, respectively, of the two-body system consisting of one star and the MBH; $r_{\rm peri} = (1-e)a$ and $r_{\rm apo} = (1+e)a$. Different colors correspond to different particles (since the total number of colors available was 12, each color is used for more than one particle). Dashed lines indicate the capture radius, $r_{\rm capt} = 8r_g$.

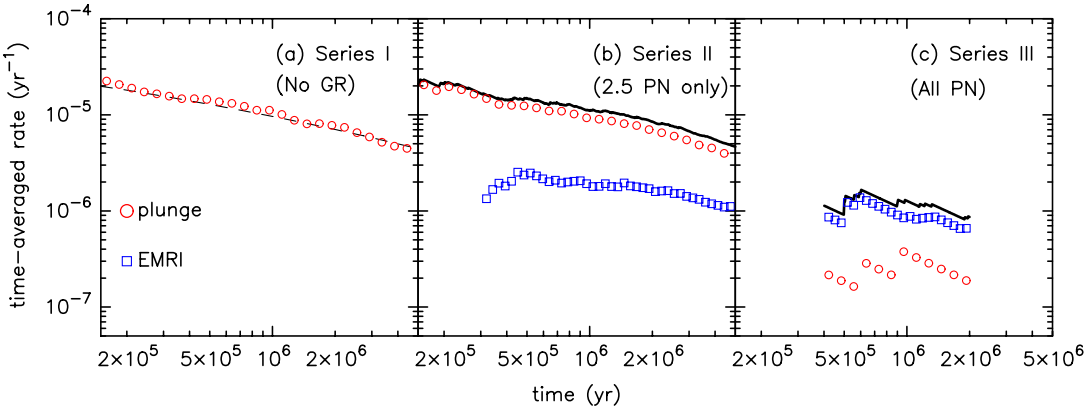

FIG. 2 (color online). Time-averaged capture rates, defined as the total number of events until time t divided by t, computed from the complete set of runs in each series. Series I: dashed line is the prediction of Eqs. (26) and (27) for $C_1 = 0.5$. The solid (black) curved lines in the Series II and Series III panels are the total event rates, EMRI plus plunges.

In this (Newtonian) regime, the mechanism expected to dominate the scattering of stars onto high-eccentricity orbits around a point mass is RR [16,20]. Because the smooth gravitational potential has symmetries that restrict the orbital evolution (i.e. to fixed ellipses in the case of a Newtonian point mass), perturbations on a test star are not random but correlated. This leads to coherent changes $\Delta\mathbf{L} = \mathbf{T}t$ on times $t \lesssim t_{\rm coh}$ by the residual torque $|\mathbf{T}| \approx \sqrt{N}Gm/r$ exerted by the N randomly oriented, orbit-averaged mass distributions of the surrounding stars. The coherence time is set by the mechanism that most rapidly causes orbits to precess, randomizing $\mathbf{T}$. In these non-relativistic simulations, that mechanism is mass precession, Eq. (15a). The accumulated change over $t_{\rm coh}$, $|\Delta L_{\rm coh}| \sim |\mathbf{T}t_{\rm coh}|$, then becomes the mean free path in $\mathbf{L}$ space for the long-term ($t \gg t_{\rm coh}$) random walk in $\mathbf{L}$. The effective relaxation time associated with RR satisfies

$$\frac{|\Delta L_{\rm coh}|}{L_c}\sqrt{\frac{t}{t_{\rm coh}}} \equiv \sqrt{\frac{t}{t_{\rm RR}}}; \tag{18}$$

i.e.

$$t_{\rm RR} = \left(\frac{L_c}{\Delta L_{\rm coh}}\right)^2 t_{\rm coh}, \tag{19}$$

where $L_c \equiv \sqrt{GM_\bullet a}$ is the angular momentum of a circular orbit with radius $r \approx a$. These relations should be understood as correct only in an order-of-magnitude sense.

In the coherent regime, the change in orbital angular momentum is

$$\left|\frac{dL}{dt}\right| \approx \sqrt{N}\frac{Gm}{a} \approx \beta_s \frac{L_c}{P}\frac{\sqrt{N}m}{M_\bullet}, \tag{20}$$

where N is roughly the number of stars within a sphere of radius a, and β_s is a dimensionless factor of order unity [29,30].

The precession time due to the distributed mass, Eq. (15a), can be written

$$t_{\rm M} \approx (1.2\times 10^4\ {\rm yr})g(e)\tilde{a}^{1/2}\left(\frac{M_\bullet}{10^6\mathcal{M}_\odot}\right)\left(\frac{M_0}{250\mathcal{M}_\odot}\right)^{-1}, \tag{21}$$

where $M_\star(<r) = M_0\tilde{r}$ and $M_0 = 250\mathcal{M}_\odot$ for the models considered here.

Identifying $t_{\rm M}$ with $t_{\rm coh}$, and writing $N(<r) = M_\star(<r)/m$, Eqs. (19)–(21) give

$$t_{\rm RR} \approx \beta_s^{-2} g(e)^{-1}\frac{M_\bullet}{m}P(a) \tag{22a}$$

$$\approx \frac{5.9\times 10^4\ {\rm yr}}{\beta_s^2 g(e)}\left(\frac{M_\bullet}{10^6\mathcal{M}_\odot}\right)^{1/2}\left(\frac{m}{50\mathcal{M}_\odot}\right)^{-1}\tilde{a}^{3/2}. \tag{22b}$$

We note that $M_\star$ has dropped out. This is only valid for values of $M_\star$ large enough that $t_{\rm coh} = t_{\rm M}$ is shorter than all other time scales of interest.

In the expression for $t_{\rm RR}$, the form of the density profile is still reflected in the dependence of g on e, which, for the assumed initial mass distribution, is strongly dependent on e as $e \to 1$ (Eq. (15b)). However, what matters for the coherence breaking is the relative precession of the test particle's orbit with respect to the other orbits. Hence, it is reasonable to average $g(e)$ in Eq. (22) over the eccentricity distribution for all the stars, Eq. (2):

$$\bar{g} \equiv \int_0^1 g(e)de^2 = \frac{3}{2}. \tag{23}$$

In what follows, we ignore changes in $\bar{g}$ due to evolution of $M_\star(r)$.

Because the integration time is long compared with $t_{\rm RR}$, we expect a quasi-steady-state to be set up in the angular momentum distribution at each a, such that the rate of loss of stars into the capture sphere is roughly equal to the rate at which new stars are being scattered onto low-angular-momentum orbits. In this regime, the (differential) rate at which stars are scattered into the MBH at each a is given approximately by:

$$\Gamma(a,t)da \approx \frac{N(a,t)da}{\ln(L_c/L_m)t_{\rm RR}} \tag{24}$$

[e.g. [31]]. The logarithmic term can be interpreted as the approximate number of relaxation times required for an orbit to diffuse in angular momentum from $e \approx 0$ to $e \approx e_m$ [32].

Using Eq. (22), the differential capture rate can be written

$$\Gamma(a,t)da = C_1\frac{m}{M_\bullet}\frac{N(a,t)da}{\ln(1-e_m^2)^{-1/2}P(a)}, \tag{25}$$

where $\beta_s^2\bar{g}$ and all other uncertainties have been absorbed into the fitting parameter C_1, assumed independent of a and t.

Equating $\Gamma(a,t)$ with $-dN(a,t)/dt$ and using Eqs. (8) and (11), the evolution equation for $N(a,t)$ becomes

$$\frac{\partial N}{\partial\tau} = -\frac{N(a,\tau)}{\tilde{a}^{3/2}\ln(a/r_{\rm capt})}, \qquad \tau \equiv t/t_1, \tag{26a}$$

$$t_1 = (5.9\times 10^4\ {\rm yr})C_1^{-1}\frac{M_\bullet/m}{2\times 10^4}\left(\frac{M_\bullet}{10^6\mathcal{M}_\odot}\right)^{-1/2}, \tag{26b}$$

with solution

$$N(\tilde{a},\tau) = N(\tilde{a},0)e^{-\tau/\tau_1}, \tag{27a}$$

$$\tau_1 = \tilde{a}^{3/2}\ln(a/r_{\rm capt}). \tag{27b}$$

Figure 3 plots the predicted, cumulative number of events versus time, compared with the results from the Series I integrations. The agreement is good for $C_1 \approx 0.5$. The mean capture rate is given by $t^{-1}\int_{a_1}^{a_2}[N(a,0) - N(a,t)]da$; this is plotted, with $C_1 = 0.5$, as the dashed line in Fig. 2(a).

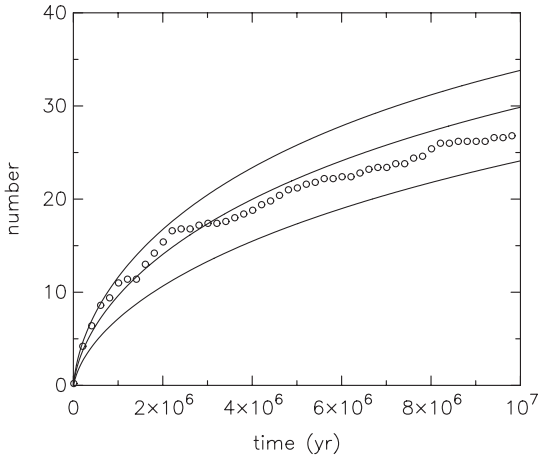

FIG. 3. Open circles show the number of stars captured up until time t in the combined runs from Series I; values are normalized to an initial total number of 50. Plotted events are all "plunges." Solid lines show the predictions of Eqs. (26) and (27) for $C_1 = (0.3, 0.5, 0.7)$.

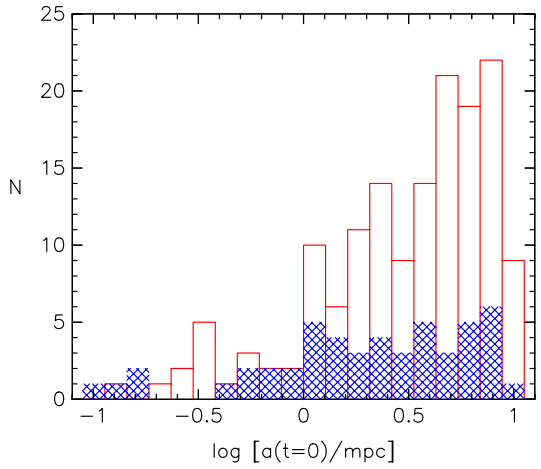

FIG. 4 (color online). Distribution of initial semi-major axes for the capture events from Series II. Red (unfilled) histogram shows the plunges; blue (crosshatched) histogram shows the EMRIs. Elapsed time is 10^7 yr.

B. Series II

Series II integrations included the 2.5 PN terms in the equations of motion, allowing some stars to be captured onto orbits that inspiral gradually into the MBH via GW energy loss.

The energy loss time scale associated with the 2.5 PN terms is [33]

$$t_{\rm GW} \equiv \left|\frac{1}{a}\frac{da}{dt}\right| = \frac{5}{64}\frac{c^5 a^4}{G^3 M_\bullet^2 m}(1-e^2)^{7/2}\left(1+\frac{73}{24}e^2+\frac{37}{96}e^4\right)^{-1} \approx 1.2\times 10^{14}\ {\rm yr}\left(\frac{m}{50\mathcal{M}_\odot}\right)^{-1}\left(\frac{M_\bullet}{10^6\mathcal{M}_\odot}\right)^{-2}\tilde{a}^4(1-e)^{7/2}, \tag{28}$$

where the latter expression assumes $e \approx 1$. In this limit, GW inspiral occurs along lines of fixed slope in the a, $(1-e)$ plane until shortly before the merger:

$$\frac{\Delta(1-e)}{1-e} \approx -\frac{\Delta a}{a}, \tag{29}$$

such that $r_p = (1-e)a$ is approximately constant [33]. In order to avoid plunging, a star must reach a high enough eccentricity that the GW time scale is shorter than the time for gravitational encounters to scatter the star onto a different orbit.

From Eqs. (IV B)-(29), the time required for GWs to change e by of order $1-e$ is $\sim t_{\rm GW}$. In the case of gravitational encounters, changes in angular momentum are equivalent to changes in eccentricity since a is nearly conserved. The time t_L for encounters to change L by of order itself is

$$(\Delta L)^2 \approx L^2 = L_c^2\frac{t_L}{t_{\rm RR}}; \tag{30}$$

i.e.

$$t_L = \left(\frac{L}{L_c}\right)^2 t_{\rm RR} \approx 2(1-e)t_{\rm RR}, \tag{31}$$

with $t_{\rm RR}$ the RR time scale defined above. Equating t_L with $t_{\rm GW}$ then gives the condition for capture onto an inspiral orbit:

$$a(1-e) \approx \frac{1}{2}\left(\frac{340\pi}{3}\right)^{2/5} r_g; \tag{32}$$

i.e. capture requires a periapse distance of $\sim 5r_g$. This is slightly smaller than the separation at which mergers were assumed to take place in the simulations (Eq. (7)).

Given the approximate nature of Eq. (32), one expects capture onto inspiral orbits for some fraction, of order unity, of stars that would otherwise plunge into the MBH. Figure 4 shows the cumulative histogram of capture events for the integrations of Series II. Roughly 1/4 (54 out of 206) events were EMRIs. Time-averaged capture rates are shown in Fig. 2(b). These results are consistent with expectations.

As shown in the next section, these results are substantially changed by the inclusion of the 1 PN and 2 PN terms into the equations of motion.

V. SERIES III

Figure 5 shows the evolution on the $(a_r, 1-e_r)$ plane of all 50 stars in an integration from Series III. Integrations in this series included all PN terms (1 PN, 2 PN, 2.5 PN). The quantities a_r, e_r are the 1 PN generalizations of the Keplerian semi-major axis and eccentricity respectively;

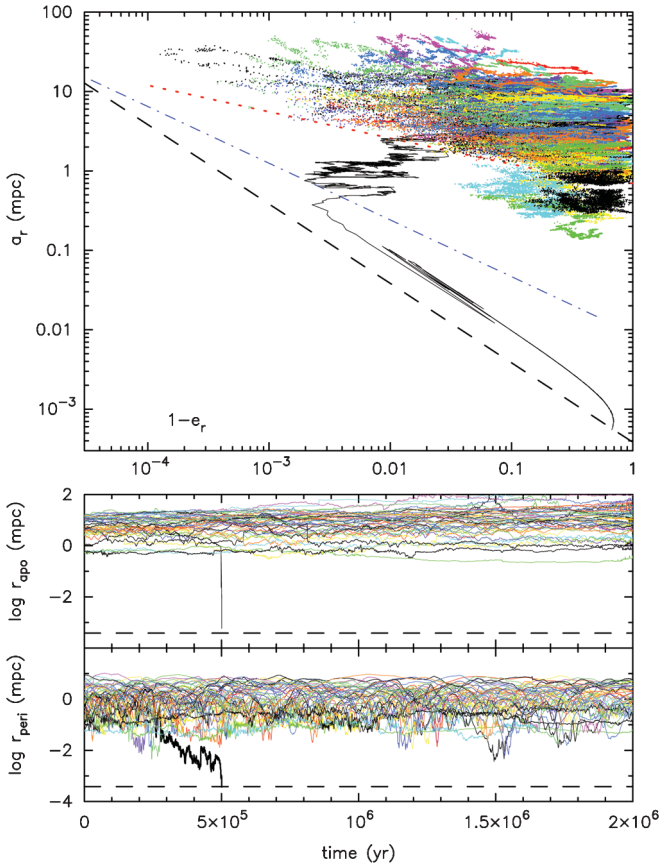

FIG. 5 (color). A simulation from Series III (all PN terms). a_r and e_r are the 1 PN generalizations of the semi-major axis and eccentricity; $r_{\rm peri} = (1 - e_r)a_r$ and $r_{\rm apo} = (1 + e_r)a_r$. Different colors correspond to different particles (the number of different colors is 12 so each color is used for more than one particle). Dashed (black) lines show the assumed capture radius, $r_{\rm capt} = 8r_g$. In the top frame, the dotted (red) line is the Schwarzschild barrier, Eq. (36), and the dash-dotted (blue) line is the approximate condition for GW capture, Eq. (62).

to this PN order, the periapse and apoapse distances are given, respectively, by $(1 - e_r)a_r$ and $(1 + e_r)a_r$ [34].

Over the course of the 2 Myr interval plotted in Fig. 5, only one capture occurs: an EMRI. The plunge events that dominated the integrations from Series I and II are absent. The mean capture rates computed from all integrations in Series III are shown in Fig. 2. The mean capture rate is $\lesssim 1\,{\rm Myr}^{-1}$, with 74% of the events EMRIs. By comparison, in Series I and II, the mean capture rate was $\gtrsim 10\ {\rm Myr}^{-1}$ at early times, and almost all events were plunges.

The proximate reason for the much lower event rate in the integrations from Series III is suggested by Fig. 5: there is an apparent barrier in orbital eccentricity, or angular momentum, which very few stars cross on Myr time scales. Furthermore, the single star that is captured in that figure appears to require a time much longer than $\sim(1 - e_r)t_{\rm RR}$ to cross the gap. The barrier is illustrated more clearly in Fig. 6, based on another integration from Series III.

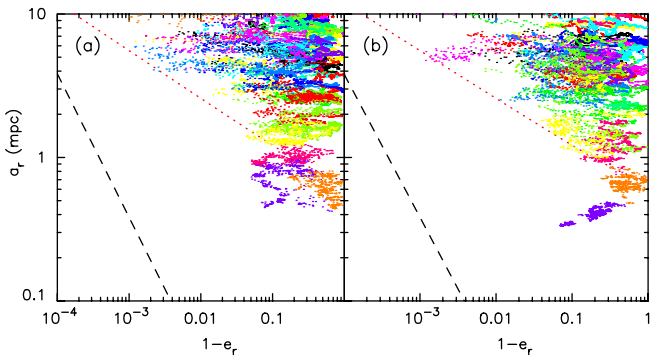

FIG. 6 (color online). Illustrating the angular momentum barrier when all PN terms are included, in two short time segments extracted from a Series III integration. (a) $4\times10^5\ {\rm yr} \le t \le 8\times10^5\ {\rm yr}$; (b) $1\times10^6\ {\rm yr} \le t \le 1.4\times10^6\ {\rm yr}$. Dashed (black) line is the capture radius; dotted (red) line is the predicted angular momentum barrier, Eq. (36). Stars that lay initially to the left of the barrier were excluded. This integration produced no EMRIs. The time interval plotted, $\Delta t = 4\times10^5$ yr, is somewhat longer than the RR time scale of Eq. (22) and much longer than $(1 - e_r)t_{\rm RR}$. Note the "barrier penetration" at small values of a_r.

This figure shows that there is some "barrier penetration" for orbits with small semi-major axis; we discuss the reasons below.

A. The Schwarzschild barrier

Adding the 1 PN terms to the equations of motion results in precession of the argument ω of orbital periapse, with an orbit-averaged frequency given by Eq. (16). For low eccentricity orbits, the rate of this Schwarzschild precession [35] is comparable to that produced by the distributed mass, Eq. (13), at the radii of interest here. But whereas the latter rate tends to zero as $e \to 1$, the Schwarzschild precession rate diverges, as $\sim(1 - e)^{-1}$. The effective time over which background torques can act is determined by the fastest mechanism that changes the relative orientation of a star with respect to the gravitational field produced by all the other stars. For a highly eccentric orbit, this mechanism is Schwarzschild precession and its associated time scale tends to zero as $e \to 1$.

We suggest that the angular momentum barrier be identified, in a qualitative way, with the value of L at which the torques become ineffective due to the orbit's rapid Schwarzschild precession.

The residual torque produced by an otherwise-spherical distribution of stars, at $r \approx a$, is of order

$$T \approx \frac{Gm}{a}\sqrt{N(a)} \approx \frac{1}{\sqrt{N(a)}}\frac{GM_\star(a)}{a}, \qquad (33)$$

where $M_\star(a) = mN(a)$ is the distributed mass within radius $r = a$. Writing $L = [GM_\bullet a(1 - e^2)]^{1/2}$ for the

angular momentum of a test star, the time scale over which this fixed torque changes L is

$$\left|\frac{1}{L}\frac{dL}{dt}\right|^{-1} \approx \sqrt{N(a)}\frac{M_\bullet}{M(a)}\left[\frac{a^3(1-e^2)}{GM_\bullet}\right]^{1/2}. \quad (34)$$

The condition that this time be shorter than the relativistic precession time, $\pi/\nu_{\rm GR}$, is

$$\ell > \ell_{\rm SB} \approx \frac{r_g}{a}\frac{M_\bullet}{M_\star(a)}\sqrt{N(a)}, \quad (35)$$

where we have written $\ell \equiv L/L_c = (1-e^2)^{1/2}$. Evaluating the quantities in Eq. (35) for the N-body models, the critical semi-major axis becomes

$$\tilde{a} = C_{\rm SB}(1-e^2)^{-1/3}, \quad (36)$$

where $C_{\rm SB}$ is a constant of order unity. Equation (36), with $C_{\rm SB} = 0.7$, is plotted as the dotted (red) lines in Figs. 5–7 and 12.

Assuming that the condition (36) holds for all values of a, the normalizing constant $C_{\rm SB}$ can be interpreted as the value of $\tilde{a}$ when $e = 0$; i.e. as the minimum value of $\tilde{a}$ for which the barrier exists. One expects that orbits with semi-major axes larger than this minimum value (and smaller than a maximum value, defined below), and that approach the barrier from the right on Figs. 5 or 6, will have a hard time crossing it, since torques become inefficient near the barrier.

We develop these ideas more quantitatively in the next subsection. Before doing so we present a more quantitative model for the behavior of low-angular-momentum orbits under the combined influence of relativistic precession and Newtonian torques.

Figure 7(a) shows the evolutionary track of a star from a Series III integration. The star first strikes the barrier at $t \approx 1.8\times10^5$ yr; the eccentricity then oscillates several times at roughly fixed amplitude before decreasing again, carrying the star away from the barrier at $t \gtrsim 2.2\times10^5$ yr. During each bounce, the argument of periapse ω advances by $\sim 2\pi$.

Many other examples of "bounce" near the angular momentum barrier were extracted from the N-body integrations. While differing in detail, all such orbits exhibited a variation in eccentricity near the barrier with a period roughly equal to the period of Schwarzschild precession.

This feature suggests that the torques responsible for angular momentum changes near the barrier are due to a distortion of the stellar potential, expressed about the location of the MBH particle, that is lopsided or dipole in character. (A quadrupole distortion would cause changes in L at twice the frequency of circulation, etc.). That the dominant component of the torquing potential should have such a form is not unreasonable, since if one represents

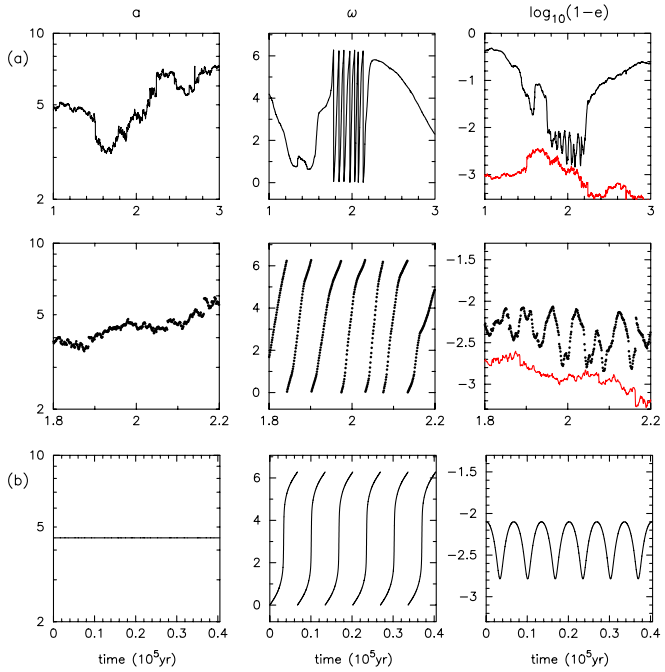

FIG. 7 (color online). (a) A bounce orbit extracted from a Series III N-body integration. Plotted are the semi-major axis, argument of periapse and eccentricity versus time, at low (upper) and high (middle) time resolutions. In the plots of eccentricity versus time, the lower (red) curved lines show the predicted location of the angular momentum barrier, Eq. (36), with $C_{\rm SB} = 0.7$. Changes in the predicted barrier location reflect changes in the semi-major axis. (b) A solution to the equations of motion (41) that reproduces the important features of the N-body orbit in (a). The duration of the bounce phase is roughly the coherence time for the background (stellar) potential. Additional details are given in the text.

the gravitational potential from N orbit-averaged stars in a multipole expansion, the largest terms are expected be the monopole (due to the spherical cluster), followed by the dipole (due to $\sqrt{N}$ departures from spherical symmetry), etc.

We also verified that the behavior of orbits like that plotted in Fig. 7 was unchanged if the mass of the test particle was drastically reduced. These tests confirmed that the variations in orbital angular momentum in the test particle's orbit were not a spurious result of motion of the black hole particle induced by the test star's precession.

We used the following simple potential to model the motion of a test star subject to a lopsided force from all the other stars:

$$\Phi(\boldsymbol{r}) = -\frac{GM_\bullet}{r} + \Phi_s V(r) - S(a)a\cos\theta. \quad (37)$$

The second term on the right-hand side of (37) is the potential of the spherical star cluster. For the models considered here,

$$V(r) = \ln\left(\frac{r}{r_0}\right), \qquad \Phi_s = \frac{GM_0}{r_0}, \qquad M_0 = M_\star(r < r_0). \tag{38}$$

The third term represents the lopsided distortion of the stellar potential; the amplitude S, which has dimensions of acceleration, is assumed to depend on the test-orbit's semi-major axis as

$$S(a) \approx \frac{Gm\sqrt{N(a)}}{a^2} \approx \frac{GM_\star(a)}{a^2\sqrt{N(a)}}. \tag{39}$$

The corresponding density is

$$\rho_D(r,\theta) = \frac{S(a)a}{2\pi G}\frac{\cos\theta}{r^2}. \tag{40}$$

The integrated mass corresponding to the lopsided component is zero.

Because of the dominance of the first term in Eq. (37), the radial period of an orbit is shorter than all other orbital time scales. In Appendix A we express the Hamiltonian corresponding to the potential (37) in terms of Delaunay action-angle variables and average over the radial motion, including the orbit-averaged term that generates the Schwarzschild precession. The result is a set of four equations that describe the rates of change of the (osculating) Keplerian elements (L, L_z, ω, Ω):

$$\frac{d\omega}{d\tau} = \ell^{-2} - A_M\ell/(1+\ell) + A_D\sin\omega\left[-\frac{\ell}{e}\sin i + \frac{e}{\sin i}\frac{\ell_z^2}{\ell^3}\right], \tag{41a}$$

$$\frac{d\ell}{d\tau} = -A_D e\sin i\cos\omega, \tag{41b}$$

$$\frac{d\Omega}{d\tau} = -A_D e\frac{\ell_z}{\ell^2}\frac{\sin\omega}{\sin i}, \tag{41c}$$

$$\frac{d\ell_z}{d\tau} = 0, \tag{41d}$$

where we have defined the dimensionless elements $\ell = L/I = \sqrt{1-e^2}$, $\ell_z = L_z/I$ and $\cos i = \ell_z/\ell$ in terms of the radial action $I = (GM_\bullet a)^{1/2}$, and the dimensionless time is $\tau \equiv \nu_0 t$, where

$$\nu_0 = \nu_r\frac{3GM_\bullet}{c^2 a}. \tag{42}$$

In defining the Delaunay variables, the plane of reference has been taken to be the (x, y) plane and the reference direction is the x-axis; thus an orbit in the (x, z) plane has $\sin i = 1$, and for such an orbit, $\omega = \pi/2$ corresponds to an orientation parallel to the z-axis, the assumed direction of the lopsided distortion. In the case of an orbit in the (x, y) plane, $\sin i = 0$, $\ell_z = \ell$, and the orientation of the orbit is determined by $\omega + \Omega$; according to Eqs. (41a) and (41c), the terms in $(d/d\tau)(\omega + \Omega)$ that are proportional to A_D sum to zero in this case.

The dimensionless parameters A_M and A_D specify the strength of the spherical and lopsided components of the distributed mass:

$$A_M = \frac{1}{3}\frac{M_\star(a)}{M_\bullet}\frac{a}{r_g}, \tag{43a}$$

$$A_D = \frac{1}{3}\frac{S}{GM_\bullet/a^2}\frac{a}{r_g} \approx \frac{1}{3\sqrt{N}}\frac{M_\star(a)}{M_\bullet}\frac{a}{r_g}. \tag{43b}$$

We note that $A_M/A_D \approx N^{1/2}$, which is of order unity in the models considered here. Thus whenever it is relevant to neglect A_M, A_D is also negligible.

After averaging, the first and third terms in Eq. (37) result in the same equations of motion as in the classical Stark problem [e.g. [36]]. The corresponding solutions [e.g. [37]] consist of circulation in Ω, with period

$$P_{\rm Stark} = \frac{4\pi}{3S}\sqrt{\frac{GM_\bullet}{a}}; \tag{44}$$

oscillations in i, e and ω have the same period, while the z-component of the angular momentum is fixed. The eccentricity reaches a maximum value that depends on L_z; for $L_z = 0$ (i.e. for $i = \pi/2$, $e_{\rm max} = 1$), while for $L_z \neq 0$ the maximum eccentricity is less than one.

In the case considered here, precession of a sufficiently eccentric orbit is dominated by the Schwarzschild term, the first term on the right-hand side of Eq. (41a). Such an orbit circulates in a nearly fixed plane and the eccentricity varies with a period equal to the period of circulation. If ℓ is sufficiently small, we can write $d\omega/d\tau \approx \langle\ell\rangle^{-2}$ with $\langle\ell\rangle$ the time-averaged angular momentum. Equations (41) then have approximate solution

$$1 - \frac{\ell(t)}{\langle\ell\rangle} \approx \langle\ell\rangle A_D\sin i\cos(\nu t), \tag{45a}$$

$$\nu = \frac{3}{c^2}\frac{(GM_\bullet)^{3/2}}{\langle\ell^2\rangle a^{5/2}}. \tag{45b}$$

In this limit, the amplitude of the angular momentum oscillations,

$$\ell_+ - \ell_- \approx 2\langle\ell\rangle^2 A_D\sin i, \tag{46}$$

decreases quadratically with $\langle\ell\rangle$.

We now return to the full equations of motion (41) in order to test whether the detailed behavior of stellar trajectories near bounce in the N-body integrations is consistent with our simple model. In the N-body models, the dimensionless parameters that appear in the equations of motion are

$$A_M \approx 1.8\tilde{a}^2, \tag{47a}$$

$$A_D \approx 1.2\tilde{a}^{3/2}, \tag{47b}$$

$$\nu_0 \approx (3.26\times 10^3\ {\rm yr})^{-1}\tilde{a}^{-5/2}; \tag{47c}$$

and the Schwarzschild precession period is

$$P_{\rm GR} \equiv \frac{2\pi}{\nu_{\rm GR}} \approx 2.1 \times 10^4 \text{ yr}(1-e^2)\tilde{a}^{5/2}. \qquad (48)$$

The N-body orbit in Fig. 7(a) exhibits ~6 full circulations in ω in a time $\sim 3.5 \times 10^4$ yr, corresponding to a precessional period of $\sim 6 \times 10^3$ yr. The semi-major axis for this star during the bounce is $3.5 \lesssim \tilde{a} \lesssim 5$ and the eccentricity is $-2.8 \lesssim \log_{10}(1-e) \lesssim -2.1$. Inserting $\tilde{a} = 4$ and $\log_{10}(1-e) = -2.5$ into Eq. (48) gives $P_{\rm GR} \approx 4 \times 10^3$ yr which is quite consistent with the observed precessional period.

Figure 7(b) shows a solution to Eqs. (41) that reproduces the other important features of the N-body orbit near bounce. We set $A_D = 10$ and $A_D = 30$ i.e., $\tilde{a} \approx 4$; the initial values of the orbital elements were $\log(1-e) = -2.1$, $\omega = -\pi/2$, $\Omega = 0$, and $i = 0.35\pi$. Variations in Ω and i (not shown here) were similar in amplitude for the N-body and numerically computed orbits.

We carried out similar comparisons for other orbits near the barrier. While differing in details, all the cases examined could be adequately represented via solutions to our simple Hamiltonian (A6).

The assumptions made in deriving the Hamiltonian (A6) are not specific to orbits near the barrier. Figure 8 summarizes the properties of orbits, of arbitrary angular momentum but restricted to the $x-z$ plane ($\sin i = \pi/2$), in the potential of Fig. 7(b). Orbits can either circulate (small angular momentum) or librate (large angular momentum). There is a critical value of the angular momentum, at the time the orbit is oriented parallel to the z-axis (i.e. the direction of the lopsided distortion), such that the precession rate $\dot{\omega} = 0$ and the orbit remains fixed in orientation; from Eq. (41a) this occurs when $\ell = \ell_{\rm crit}$ where

$$0 = 1 - A_{\rm M}\frac{\ell_{\rm crit}^3}{1+\ell_{\rm crit}} - A_D\frac{\ell_{\rm crit}^3}{\sqrt{1-\ell_{\rm crit}^2}} \qquad (49)$$

or $\ell_{\rm crit} \approx 0.310$ in Fig. 8. Away from this value, librating orbits experience both their minimum and maximum angular momenta when precessing past the z-axis; first in one sense (when the mass precession term dominates) and then in the other (when the Schwarzschild term dominates). Libration changes to circulation when the orbit precesses by an angle $\pm\pi$ from its starting point along the z-axis. The minimum angular momentum reached by the orbit at the libration/circulation boundary is labeled $\ell_{\rm min}$ on Fig. 8; in this potential, $\ell_{\rm min} \approx 0.045$.

Figure 9 shows two orbits from this plane, one circulating and one librating. We note here one property common to both types of orbit: stars tend to spend more time with high angular momentum than with low angular momentuml. The reasons for this behavior are apparent in the equations of motion (41). (1) For large ℓ, $d\ell/d\tau$ is small; i.e. the orbit-averaged effects of the torque are small. (2) Orbits tend to linger at values of ω corresponding to large ℓ since the Schwarzschild precession rate is proportional to ℓ^{-2}. (The latter trend reverses for orbits so circular that mass precession dominates the Schwarzschild precession.)

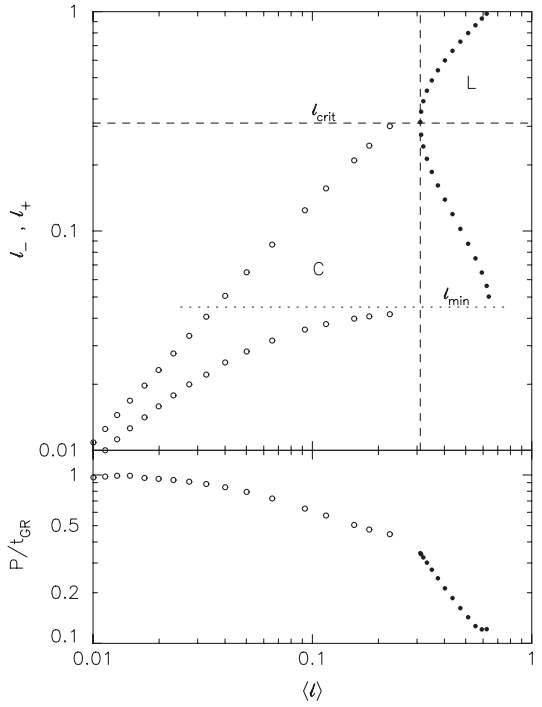

FIG. 8. Properties of two-dimensional ($\sin i = \pi/2$) solutions to the equations of motion (41), with $A_{\rm M} = 30$, $A_D = 10$. $\langle\ell\rangle$ is the dimensionless angular momentum, $\ell = \sqrt{1-e^2}$, averaged over one precessional or librational period P. *Top panel:* minimum and maximum angular momenta reached by the orbit over one period. Filled circles ("L") are librating orbits while open circles ("C") are circulating orbits. The dashed lines at $\ell = \ell_{\rm crit}$ mark the angular momentum at which the precession rate, $d\omega/dt$, is zero. The dotted line marked $\ell_{\rm min}$ is the minimum angular momentum reached by librating orbits; it is argued in the text that this is essentially the angular momentum corresponding to the Schwarzschild barrier, Eq. (35). *Bottom panel:* Librational/precessional periods as a fraction of the Schwarzschild period, computed from Eq. (16) after replacing $(1-e^2)$ by $\langle\ell\rangle^2$.

Combining Eqs. (35) and (43b),

$$\ell_{\rm SB} \approx (2A_D)^{-1} \qquad (50)$$

or $\ell_{\rm SB} \approx 0.05$ for $A_D = 10$. Not coincidentally, this is roughly equal to $\ell_{\rm min} \approx 0.045$. Figure 8 shows that $\ell_{\rm min}$ specifies not only the minimum angular momentum achievable by librating orbits, but is also roughly the minimum ℓ reached by orbits whose angular momentum changes by of order itself over one period; these were the two assumptions made in deriving (35).

At the same time, it is clear from Fig. 8 that orbits with $\ell_- \ll \ell_{\rm min}$ do exist. Apparently, such orbits are rarely reached in the N-body integrations. We discuss the reasons in the next subsection.

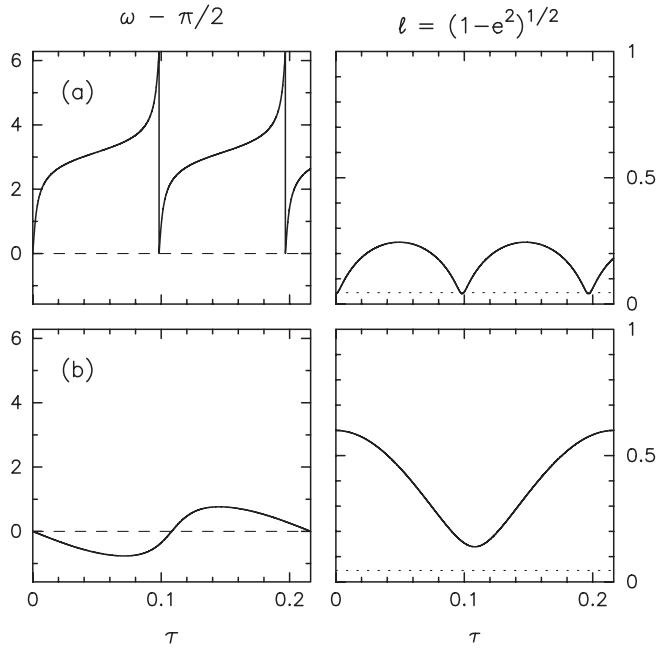

FIG. 9. Two orbits from Fig. 8. (a) $\langle \ell \rangle = 0.225$ (circulating); (b) $\langle \ell \rangle = 0.402$ (librating). $\omega = \pi/2$ corresponds to orientation along the z axis. The dotted lines in the right-hand panels indicate $\ell_{\rm min}$.

B. Barrier penetration. I

Here we address the question of how orbits evolve after striking the angular momentum barrier. The mechanism (''tunneling'') explored in this section, which is based on RR, will turn out to be less important as a source of barrier penetration than the mechanism presented in the next section, based on non-resonant relaxation (NRR). We nevertheless explore it in some detail since doing so will lead to insights about why the barrier is so ''hard'' on time scales comparable to the RR time.

The Hamiltonian model just presented assumed a fixed gravitational potential. The (constant) term responsible for the torques was assumed to arise from the time-averaged potential of the N stars. In reality, the background potential must change as the orbits of all the stars evolve (e.g. precess), leading to quasi-random changes in the direction and amplitude of the torque that acts on a single star. The changes in the background torques are responsible both for moving a star toward the barrier and moving it away. As we show here, such changes can also result in barrier penetration.

In Sec. IV, the mass precession time,

$$t_{\rm M} \equiv \frac{\pi}{|\nu_{\rm M}|} \approx 1.8 \times 10^4 \ {\rm yr} \tilde{a}^{1/2} \left(\frac{M_\bullet}{10^6 \mathcal{M}_\odot}\right)\left(\frac{M_0}{250 \mathcal{M}_\odot}\right)^{-1}, \tag{51a}$$

was taken as the ''coherence time'' over which the background torques can be assumed constant. We emphasize that the relevant time here is the precession time for a typical orbit, hence we have set $g(e) = \bar{g} = 3/2$ in Eq. (21); the fact that some (high-e) orbits precess much faster due to relativity is not important.

A second relevant time scale is the so-called vector resonant relaxation (VRR) time, the time for orbital planes to change due to their mutual torques [e.g. [15]]:

$$t_{{\rm RR},v} \approx \frac{\pi}{\nu_r} \frac{M_\bullet}{m\sqrt{N}} \approx 1.3 \times 10^4 \ {\rm yr} \tilde{a} \left(\frac{M_\bullet}{10^6 \mathcal{M}_\odot}\right)^{-1} \left(\frac{\tilde{N}}{5}\right)^{-1/2}, \tag{52}$$

where we have written $\tilde{N} = N(<\tilde{a})/\tilde{a}$; $\tilde{N} \approx 5$ in the N-body models. Since $t_{\rm M} \approx t_{{\rm RR},v}/\sqrt{N}$, one normally assumes $t_{\rm M} \ll t_{{\rm RR},v}$. However, the small values of N considered here, together with the approximate nature of Eq. (52), means that the two time scales are essentially the same in these models at all radii of interest. Furthermore, VRR leads to full randomization of orbital orientations in the sense that it changes orbital planes as well as orientations within the plane; mass precession leaves the orbital planes unchanged. For these reasons, we adopt $t_{{\rm RR},v}$ as the coherence time in the remainder of this section.

The time-independent model presented above implicitly assumed that $t_{\rm coh}$ was long compared with orbital precessional periods. In fact, the ratio of the coherence time to the Schwarzschild precession time is

$$\frac{t_{\rm coh}}{t_{\rm GR}} \approx 3 \frac{r_g}{a} \frac{M_\bullet}{m} \frac{1}{\sqrt{N}} \frac{1}{1-e^2} \tag{53a}$$

$$\approx \frac{3}{2} A_D^{-1} (1-e^2)^{-1}. \tag{53b}$$

Using Eq. (35) to relate a to e along the barrier,

$$\left(\frac{t_{\rm coh}}{t_{\rm GR}}\right)_{\rm SB} \approx 3 \frac{a}{r_g} \frac{m}{M_\bullet} \sqrt{N} \tag{54a}$$

$$\approx 6 A_D \approx 7.2 \tilde{a}^{3/2}, \tag{54b}$$

where the final expression refers to the N-body models and uses Eq. (47b). Equations (54) suggest that for orbits near the barrier with $\tilde{a} \gtrsim 1$ the background potential should remain constant for several Schwarzschild precessional periods. This is consistent with the observed behavior of orbits like the one in Fig. 7(a) ($\tilde{a} \approx 4$), which precesses a few times before (presumably) changes in the background potential cause the orbit to evolve away from the barrier. In the case of orbits with $\tilde{a} \lesssim 1$, the two time scales can be assumed to be comparable in our models.

One way to penetrate the barrier is suggested by Fig. 8. Random changes in the background potential (e.g. in the direction of the lopsided term) could have the effect of moving orbits progressively to the left and downward on that plot. This is because the minimum angular momentum reached by an orbit over a precessional period, ℓ_-, depends both on the instantaneous value of ℓ, and on the relative orientation of the orbit and the torquing term. A sequence

of correlated changes in the direction of the torque could result in gradual transition down the narrow "neck" at the lower left of the diagram, toward arbitrarily small values of $\langle\ell\rangle$.

This mechanism can be simply modeled if we assume that (1) changes in the background potential are instantaneous, separated by time $\sim t_{\rm coh}$, and (2) $t_{\rm coh} \gg t_{\rm GR}$, so that the orbital phase is essentially random at the time that the potential changes. The first assumption is not likely to be satisfied in all cases and we relax it below; however, we will argue that it corresponds to the highest probability for barrier penetration.

Consider first the two-dimensional case; i.e. $\sin i = \pi/2$. Assume as well that the orbit is sufficiently far down the neck that the angular momentum follows Eq. (45),

$$\ell^0(\omega) \approx \langle\ell\rangle^0[1 - \langle\ell\rangle^0 A_D \cos(\omega - \omega_D^0)], \qquad (55)$$

where ω_D^0 is the initial orientation of the lopsided distortion. Now let the direction of the distortion instantaneously change, to ω_D^1. The new orbit follows

$$\ell^1(\omega) \approx \langle\ell\rangle^1[1 - \langle\ell\rangle^1 A_D \cos(\omega - \omega_D^1)]. \qquad (56)$$

If the change occurs when $\omega = \omega^1$, then

$$\langle\ell\rangle^1[1 - \langle\ell\rangle^1 A_D \cos(\omega^1 - \omega_D^1)] = \langle\ell\rangle^0[1 - \langle\ell\rangle^0 A_D \cos(\omega^0 - \omega_D^0)]. \qquad (57)$$

The change in $\langle\ell\rangle$, $\Delta\langle\ell\rangle \equiv \langle\ell\rangle^1 - \langle\ell\rangle^0$ is

$$\Delta\langle\ell\rangle \approx -\langle\ell\rangle^2 A_D[\cos\delta(1 - \cos\Delta) - \sin\delta\sin\Delta], \qquad (58)$$

where $\delta = \omega^1 - \omega_D^0$ and $\Delta = \omega_D^1 - \omega_D^0$; in this simple model, both angles are random variables. Decreases in $\langle\ell\rangle$ are clearly allowed, although the amplitude of the step size becomes increasingly small, $\Delta\langle\ell\rangle \sim \langle\ell\rangle^2$, as $\langle\ell\rangle$ decreases.

There is an additional reason why evolution toward small $\langle\ell\rangle$ is disfavored. Equations (55) assume a constant rate of circulation in ω and ignore the eccentricity dependence of the averaged torque, Eq. (41c). But as noted above, away from the limit of small $\langle\ell\rangle$, orbits violate both assumptions, and tend to linger at high values of ℓ. As a result, changes in the potential are most likely to occur when ℓ is large.

For these two reasons, we do not expect the mechanism discussed in this section to be effective at moving stars very far to the left of the Schwarzschild barrier; indeed we will argue in a subsequent paper [38] that evolution to lower ℓ via this mechanism is exponentially suppressed (and this is the basis for assigning the name tunneling.) However, the ineffectiveness of RR at breaching the barrier is important in explaining why the barrier is observed to be so "hard," at least on time scales comparable to $t_{\rm RR}$.

We tested this model of barrier penetration using a Monte-Carlo code. The 3d equations of motion (41) were re-derived for an arbitary orientation of the lopsided distortion. Starting from some randomly-chosen initial values, an orbit was evolved in this fixed potential for a time $t_{\rm coh}$. The orientation of the lopsided distortion was then randomized and the integration was continued in the new potential, followed by another randomization of the potential, etc. In addition to the parameters A_D, $A_{\rm M}$ defined in Eqs. (43) and (47), this Monte-Carlo model has the additional parameter

$$R \equiv \nu_0 t_{\rm coh} = \frac{3\pi}{2A_D} \approx 4\tilde{a}^{-3/2}, \qquad (59)$$

the dimensionless time between potential reorientations, where the final expression uses Eq. (47b). The number of Schwarzschild precessional periods between potential re-orientations is $\sim R/2\pi\langle\ell\rangle^2$.

Monte-Carlo experiments were carried out for the following sets of parameters:

$$A_{\rm M} = 7, \quad A_D = 3, \quad R = 1.4(\tilde{a} \approx 2)$$
$$A_{\rm M} = 30, \quad A_D = 10, \quad R = 0.5(\tilde{a} \approx 4)$$
$$A_{\rm M} = 120, \quad A_D = 30, \quad R = 0.2(\tilde{a} \approx 8).$$

For each choice of parameters, 1000 Monte-Carlo experiments with different initial seeds were carried out, and each experiment embodied 1000 re-orientations of the potential.

Figure 10 shows the resulting, time-averaged angular momentum distributions. Also plotted there is the expected location of the Schwarzschild barrier, computed using Eq. (50). While the latter is by nature approximate, Fig. 10 reveals a tail toward low angular momenta rather than a sharp cutoff at any value of ℓ; orbits sometimes reach values of ℓ that are $\sim$ an order of magnitude smaller than the predicted $\ell_{\rm SB}$.

The angular momentum distributions in the N-body integrations are shown in Fig. 11. At all radii, there is a sharp cutoff in the distribution at some value of $(1 - e)$. At large distances, $\tilde{a} = 4$ and 8 (this cutoff lies close to $\ell = \ell_{\rm SB}$), while at smaller radii, the distribution extends beyond the expected barrier location (see also Fig. 6). By comparison, while the angular momentum cutoff in the Monte-Carlo experiments is also quite sharp, it occurs at ℓ values that are somewhat lower than $\ell_{\rm SB}$ for all values of a.

The assumption that the potential changes suddenly every $\sim t_{\rm coh}$ is unrealistic. In reality, changes in the background potential are due to the combined precession of individual orbits, which is a gradual process. One consequence is that adiabatic invariance will be respected for orbital actions whose conjugate angles are varying on time scales much shorter than $t_{\rm coh}$. This is not the case if the potential changes instantaneously, as in the model just considered. For instance, if the period of Schwarzschild precession of an orbit is short compared with $t_{\rm coh}$, its angular momentum will be nearly conserved. From Eq. (54), this condition is satisfied for N-body orbits near

the barrier when $\tilde{a}$ is sufficiently large; e.g. for $\tilde{a} = 4$, $t_{\rm coh}/t_{\rm GR} \approx 60$. For $\tilde{a} \leq 1$, this ratio is $\lesssim 10$, suggesting that adiabatic invariance will not be strictly enforced. This is a plausible explanation for the better success of the Monte-Carlo model at smaller radii.

To test this idea, we carried out a second set of Monte-Carlo experiments in which changes in the background potential were continuous with respect to time. The total change in the orientation of the torquing potential after each $t_{\rm coh}$ was the same as in the first set of experiments, but now the vector describing the distortion was rotated at a fixed rate, along a great circle, from its initial to final orientations during each interval.

Figure 10 shows the results. As expected, the angular momentum distributions are now truncated more sharply at small values. In the case of $\tilde{a} = 8$, the distribution falls to zero at $\ell \approx \ell_{\rm SB}$. As $\tilde{a}$ is decreased, the distributions extend progressively farther below the barrier, approaching more closely to the results of the first set of experiments. These distributions are quite consistent with those from the N-body models, Fig. 11.

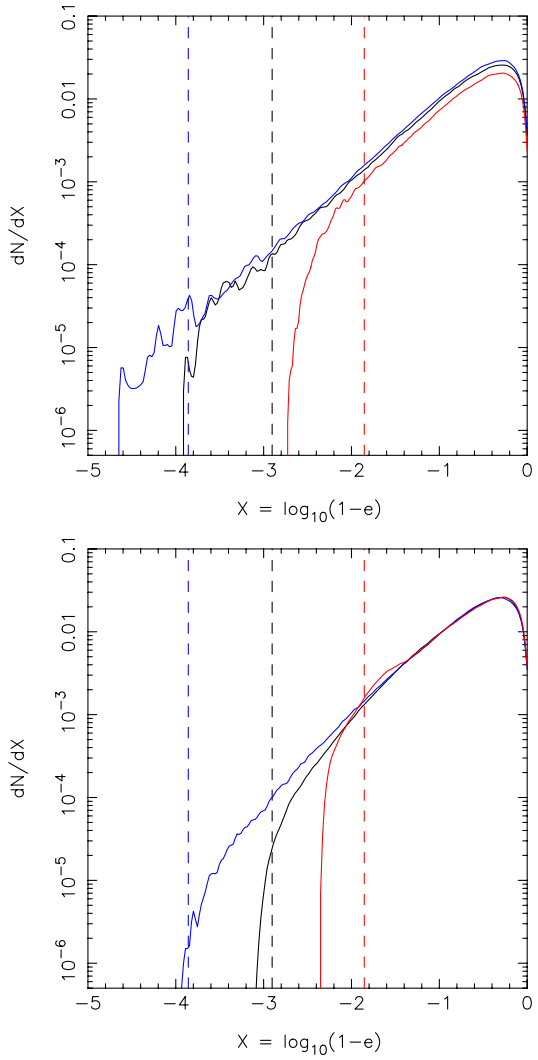

FIG. 10 (color online). Angular momentum distributions from Monte-Carlo simulations in which the potential was re-oriented suddenly (top panel) or smoothly (bottom panel) each $t_{\rm coh}$. *Red line (rightmost):* $\tilde{a} = 2$; *black:* $\tilde{a} = 4$; *blue line (leftmost):* $\tilde{a} = 8$. Dashed lines show the predicted barrier location, Eq. (50).

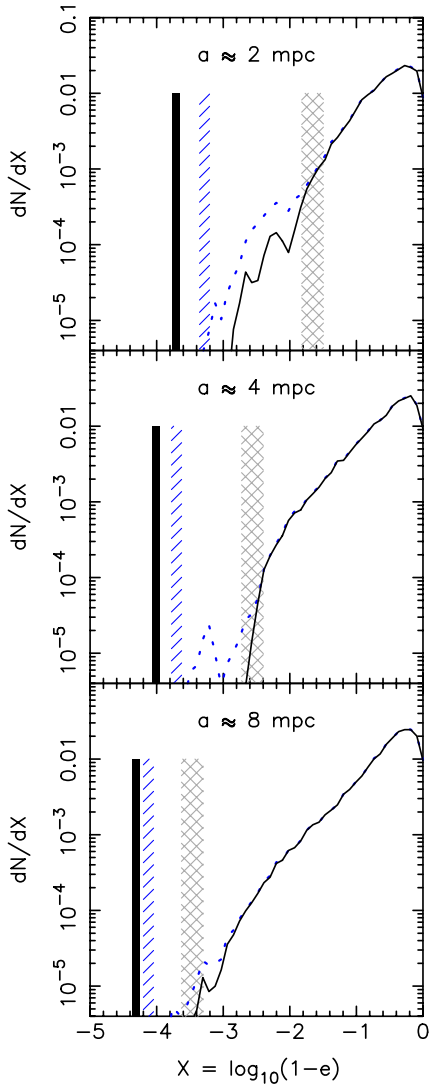

FIG. 11 (color online). Time-averaged angular momentum distributions of stars in the Series III N-body integrations, in three intervals of semi-major axis. The distributions were computed using all stars with instantaneous $\tilde{a}$ values in a range $\Delta\log_{10}\tilde{a} = \pm 0.05$ centered on the stated value, over the time interval $0 \leq t \leq 2 \times 10^6$ yr. The solid (black) curved lines exclude stars that eventually become EMRIs; the dotted (blue) curved lines include these stars. Crosshatched (grey) areas show the predicted location of the Schwarzschild barrier, Eq. (36), given the lower and upper limits on $\tilde{a}$. Hatched (blue) areas show the capture angular momentum for EMRIs, Eq. (62). Solid rectangles show the angular momentum at the assumed capture radius around the MBH.

As noted above, the semi-empirical criterion (36) implies that there is a minimum value of a, $\tilde{a} \lesssim C_{\rm SB} \approx 0.7$ using the adopted value of $C_{\rm SB}$, below which there is no barrier. A straightforward prediction is that stars with initial values of the semi-major axis below $\sim$0.7 mpc should be able to form EMRIs, at a rate that is unaffected by the arguments presented in this section. We show below that this is in fact the case.

Nevertheless, a robust result of the work presented in this section is that RR itself is ineffective at coaxing stars much past the Schwarzschild angular momentum barrier. Rather, these results imply that the barrier should be "hard," at least on time scales comparable with $t_{\rm RR}$ or $t_{\rm coh}$, or 10^4–10^5 yr in these simulations.

C. Barrier penetration. II

As noted above (cf. Figure 2), one or two stars per Myr were captured by the MBH, on average, in the Series III integrations, most of them as EMRIs. Fig 12 shows several examples.

In Newtonian systems, classical, "two-body" (non-coherent) scattering is much less effective than RR at changing stars' angular momenta when the motion is nearly Keplerian. But this is not necessarily the case for stars on orbits near or beyond the Schwarzschild barrier, where RR is effectively quenched by the rapid relativistic precession. In this section we consider the extent to which classical, or non-resonant (NR), relaxation can explain the EMRI events in the N-body integrations.

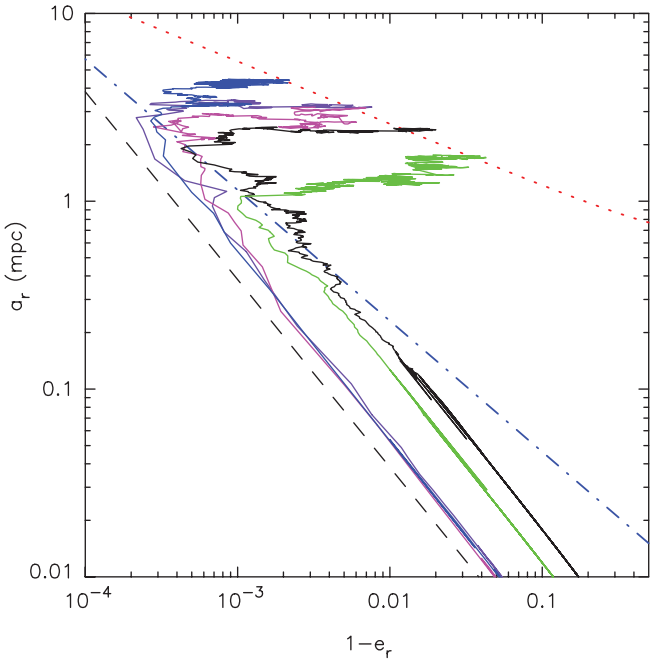

FIG. 12 (color). Evolutionary tracks for a subset of the stars from Series III integrations that became EMRIs. Dotted (red) line is the Schwarzschild barrier, Eq. (36). Dash-dotted (blue) line is Eq. (62), a prediction for the critical eccentricity at which GW energy loss dominates the evolution, assuming that the gravitational perturbations are dominated by NRR. Dashed (black) line shows the assumed capture radius.

The orbit-averaged NR relaxation time $t_{\rm NR}$ for stars of semi-major axis a in our model (a $n \propto r^{-2}$ density cusp around a MBH) is

$$t_{\rm NR} \approx 4.6\ {\rm Myr}\tilde{a}^{1/2}\left(\frac{M_\bullet}{10^6\mathcal{M}_\odot}\right)^{3/2}\left(\frac{m}{50\mathcal{M}_\odot}\right)^{-2}\left(\frac{\tilde{N}}{5}\right)^{-1}, \quad (60)$$

with $\tilde{N}$ the number of stars within 1 mpc (Appendix B).

Suppose that NR were the only mechanism capable of changing stars' angular momentum leftward of the Schwarzschild barrier. The condition for capture onto a GW-dominated orbit would then be obtained by replacing $t_{\rm RR}$ by $t_{\rm NR}$ in Eq. (31):

$$t_{\rm GW} = 2(1-e)t_{\rm NR}. \quad (61)$$

We find from Eqs. (IV B), (60) and (61) the critical value of $\tilde{a}$ at which this condition is satisfied:

$$\tilde{a}_{\rm GW} = 2.0\tilde{r}_g^{5/7}\left(\frac{M_\bullet}{m\tilde{N}\ln\Lambda}\right)^{2/7}(1-e)^{-5/7}$$
$$\approx 9\times10^{-3}\left(\frac{M_\bullet}{10^6\mathcal{M}_\odot}\right)\left(\frac{m}{50\mathcal{M}_\odot}\right)^{-2/7}\left(\frac{\tilde{N}}{5}\right)^{-2/7}(1-e)^{-5/7}, \quad (62)$$

where $\tilde{N}$ is the number of stars with $a \le 1$ mpc.

Equation (62) is plotted as the dot-dashed (blue) line in Fig. 12. After crossing this line, stars can be seen to remain near to it for some time as their energy drops. This diagram suggests that Eq. (62) accurately specifies the region where GW approximation for the electron self-energy (GW) energy loss and gravitational scattering are equally important, consistent with our assumption that NR relaxation is the dominant mechanism for angular momentum evolution in this part of the (a, e) diagram.

Given a criterion for when a star enters the GW regime, we can then ask how often the barrier penetration described in the previous section would have resulted in EMRIs.

Before doing so, we note two characteristic radii associated with $a_{\rm GW}$. When

$$a \gtrsim 0.8\ {\rm mpc}\left(\frac{M_\bullet}{m}\right)^{1/3}\left(\frac{M_\bullet}{10^6\mathcal{M}_\odot}\right)^{-5/8}\tilde{N}^{-1/24}, \quad (63)$$

the Schwarzschild barrier lies to the left of the GW line. In the N-body models considered here, the critical value is $\tilde{a} \approx 20$ beyond $\tilde{a}_{\rm max} = 10$. At and above such radii, the Schwarzschild barrier would not be an impediment to EMRI formation, and the EMRI rate (per interval of semi-major axis) would be similar to what was found above in the Series II integrations. This limit is probably of only academic interest, however, since in standard models of nuclei, almost all EMRIs would originate from orbits with $\lesssim 0.01$ pc.

At the other extreme in radius, the Schwarzschild barrier lies to the right of $e = 0$. In the N-body models, the

intersection occurs at $\tilde{a} = C_{\rm SB} \approx 0.7$; in general, Eqs. (35) and (62) give for this condition

$$a \lesssim 1.6 \times 10^{-3}\ {\rm pc}\left(\frac{M_\bullet}{m}\right)^{2/3}\tilde{N}^{-1/3}. \tag{64}$$

Since the barrier does not exist at these radii, the differential capture rates would also be similar to what was observed in the Series III simulations.

For values of the semi-major axis between these two extremes ($0.7 \lesssim \tilde{a} \lesssim 10$ in the N-body models), the Schwarzschild barrier exists and lies to the right of the critical eccentricity for GW emission. EMRI formation at these radii requires a substantial degree of barrier penetration.

We tabulated how often in the Monte-Carlo experiments from the previous section a star passed the GW boundary. Since not every experiment resulted in such an event, the mean event time, in each set of experiments, was computed using a formula from survival analysis [39]:

$$\bar{t} = \frac{1}{N_e}\sum_{i=0}^{N_e} t_i + \frac{N_{\rm MC} - N_e}{N_e}T, \tag{65}$$

where $N_{\rm MC}$ is the total number of experiments, N_e is the number of experiments in which the star satisfied the condition (62) at least once, t_i is the time at which this first occurred, and T is the total elapsed time per experiment.

The results are presented in Table I, for the first (sharp changes, $\bar{t}_1$) and second (smooth changes, $\bar{t}_2$) sets of Monte-Carlo experiments. As expected, for large $\tilde{a}$, the two times are similar since the barrier is no impediment. At smaller radii, the mean times are interestingly short only in the first set of experiments; in the second set, no events were observed. We note a certain ''conspiracy'': at small a, the degree of barrier penetration is greater, but the GW line lies farther from the Schwazschild barrier.

Next we consider the effectiveness of NRR at penetrating the barrier. Several factors are relevant:

(1) Because RR is so rapid to the right of the barrier, the angular momentum distribution in this region should remain close to that associated with an isotropic phase-space density; i.e. $N(\ell)d\ell \approx$ constant $\times\, \ell d\ell$. This contrasts with the case [e.g. [31]] where NR alone determines the phase space density, leading to a logarithmic decrease in N with respect to ℓ near the loss-cone boundary.

TABLE I. Mean times to EMRI formation in the Monte-Carlo experiments

$\tilde{a}$	$\bar{t}_1$ (yr)	$\bar{t}_2$ (yr)
2	3.1×10^8	...
4	2.8×10^8	...
8	1.2×10^8	1.5×10^8

(2) The angular momentum of a star near the barrier oscillates, at roughly the Schwarzschild frequency, with amplitude $\delta\ell = \ell_+ - \ell_- \approx \ell_+ - \ell_{\rm SB}$ (Eq. (46)). To push a star past the barrier, a NR perturbation will require a finite amplitude $\Delta\ell_{\rm NR} \gtrsim \delta\ell$.

(3) Stars remain near the barrier only for a time $\sim t_{\rm coh}$; after this, the direction of the background torque changes, and the star random-walks to larger angular momenta, as discussed in the previous section.

The change in ℓ due to NR over an interval of time equal to $t_{\rm coh}$ is

$$(\Delta\ell)_{\rm NR} \approx \left(\frac{t_{\rm coh}}{t_{\rm NR}}\right)^{1/2}. \tag{66}$$

This change is large enough to move a star leftward of the barrier if

$$(\Delta\ell)_{\rm NR} \gtrsim \delta\ell = \ell_+ - \ell_{\rm SB} \approx \ell_+ - \ell_- \approx 2\langle\ell\rangle^2 A_D. \tag{67}$$

Let $\ell_{\rm max}(a)$ be the largest value of ℓ_+ for which this condition is satisfied. Writing

$$\ell_+ \approx \langle\ell\rangle + \frac{1}{2}(\ell_+ - \ell_-) \approx \langle\ell\rangle + \langle\ell\rangle^2 A_D \tag{68}$$

and eliminating $\langle\ell\rangle$ in Eqs. (67) and (68) then gives

$$\ell_{\rm max} \approx \frac{1}{2}(\Delta\ell)_{\rm NR} + (2A_D)^{-1/2}(\Delta\ell)_{\rm NR}^{1/2}. \tag{69}$$

At every a, we expect stars with $\ell_+ \lesssim \ell_{\rm max}(a)$ to be scattered leftward of the barrier in a time $t_{\rm coh}$. The fraction of stars at a with $\ell_{\rm SB}(a) \le \ell \le \ell_{\rm max}(a)$ is

$$F(a) \approx \ell_{\rm max}^2(a) - \ell_{\rm SB}^2(a) \tag{70}$$

and the time scale for stars to be lost past the barrier is therefore

$$t_{\rm loss}(a) \equiv \left|\frac{1}{N}\frac{dN}{dt}\right|^{-1} \approx F(a)^{-1}t_{\rm coh}(a). \tag{71}$$

We evaluate $(\Delta\ell)_{\rm NR}$ using each of the two choices for $t_{\rm coh}$ discussed above: the mass precession time, Eq. (51a), which gives

$$(\Delta\ell)_{\rm NR,M} \approx 4.4 \times 10^{-2} \tag{72}$$

in the N-body models; and the VRR time, Eq. (52), for which

$$(\Delta\ell)_{\rm NR,RR\nu} \approx 5.3 \times 10^{-2}\tilde{a}^{1/4}. \tag{73}$$

Tables II and III give the computed values of F and $F^{-1}t_{\rm coh}$ for the two choices of $t_{\rm coh}$. Predicted loss rates are similar for high a values, and in both cases, NR is predicted to fail to breach the barrier when $\tilde{a} \lesssim 2$–3.

Figure 13 plots histograms of the capture events in the Series III integrations. As predicted, the number of events falls sharply for $\tilde{a} \lesssim 2$–3 mpc. A few captures also occur

TABLE II. NR loss rates: $t_{\rm coh} = t_{\rm M}$.

$\tilde{a}$	$t_{\rm coh}$ (yr)	$\ell^2_{\rm max} - \ell^2_{\rm SB}$	$t_{\rm loss}$ (yr)
2	1.2×10^4	...	...
3	1.6×10^4	4.9×10^{-5}	3.1×10^8
4	1.8×10^4	2.1×10^{-3}	8.5×10^6
5	2.0×10^4	2.5×10^{-3}	8.1×10^6
6	2.2×10^4	2.5×10^{-3}	8.9×10^6
8	2.5×10^4	2.2×10^{-3}	1.2×10^7
10	2.8×10^4	1.9×10^{-3}	1.5×10^7

TABLE III. NR loss rates: $t_{\rm coh} = t_{{\rm RR},v}$.

$\tilde{a}$	$t_{\rm coh}$ (yr)	$\ell^2_{\rm max} - \ell^2_{\rm SB}$	$t_{\rm loss}$ (yr)
2	2.6×10^4	...	...
3	3.9×10^4	5.6×10^{-3}	7.2×10^6
4	5.2×10^4	7.2×10^{-3}	7.4×10^6
5	6.5×10^4	7.5×10^{-3}	9.0×10^6
6	7.8×10^4	7.3×10^{-3}	1.1×10^7
8	1.4×10^5	6.9×10^{-3}	1.5×10^7
10	1.3×10^5	6.6×10^{-3}	2.0×10^7

from orbits with $\tilde{a} \lesssim 1$, roughly the minimum value for which the barrier is present.

We can also compare predicted and measured event rates. From Fig. 2, the mean capture rate at early times in the Series III integrations is $\sim 1 - 2 \times 10^{-6}$ yr^{-1}. (Four out of 19 of the events were associated with orbits below the Schwarzschild barrier, reducing the mean rate of barrier-crossing events slightly.) The number of stars initially with $\tilde{a} \gtrsim 2$–3 is ~35–40, and the loss times in Table II are roughly 1×10^7 yr at these radii. The predicted event rate is therefore 3–4 $\times 10^{-6}$ yr^{-1}—in reasonable agreement with the measured values given the crudeness of the model. We note that our model can be expected to overestimate the capture rate since it ignores the possibility of a star returning to the right of the barrier after crossing it.

We will present a more detailed calculation of the barrier penetration rate due to NR in a later paper [38].

VI. DISCUSSION

Here we discuss briefly how the key results from the N-body experiments can be extended to nuclear star clusters with more general properties. We treat this topic in more detail in Papers II and III [38,40]. In particular, we do not attempt here to derive absolute EMRI rate estimates for general clusters.

We begin by collecting some of the important relations derived above and expressing them in more general form.

Combining the parameter dependence of Eq. (35) with the empirical normalization of Eq. (36), we find for the angular momentum that defines the Schwarzschild barrier:

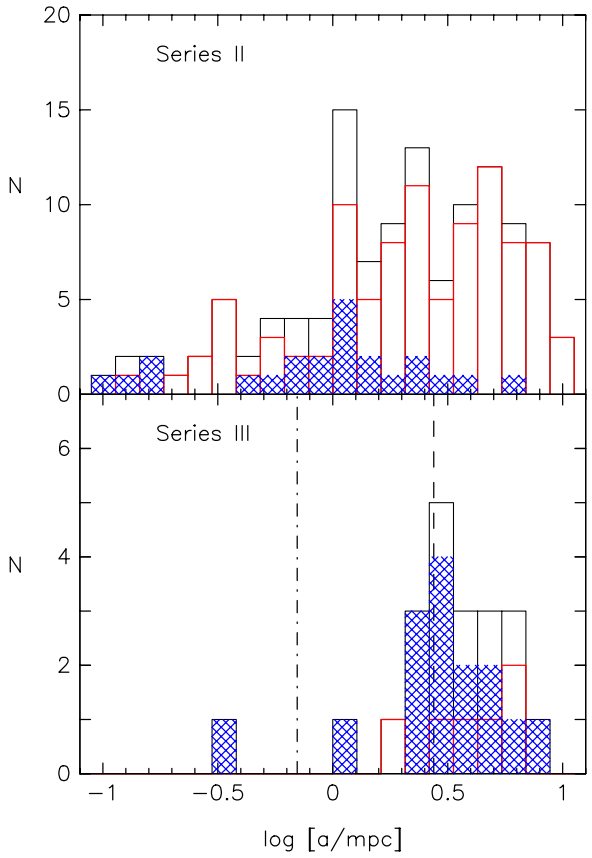

FIG. 13 (color online). Distribution of semi-major axes for the capture events from Series II (top) and Series III (bottom). Red (unfilled) histogram shows the plunges; blue (crosshatched) histogram shows the EMRIs; the total is indicated in black. In the upper panel, the initial value of a is used; in the lower panel, the value of a during the final crossing of the Schwarzschild barrier was used. In both panels, the elapsed time is 2×10^6 yr. To the left of the dashed vertical line in the lower panel, NRR is predicted to be ineffective at pushing stars past the Schwarzschild barrier. To the left of the dash-dotted vertical line, the Schwarzschild barrier does not exist.

$$(1-e^2)_{\rm SB} \approx 1.9\left(\frac{C_{\rm SB}}{0.7}\right)^2\left(\frac{r_g}{a}\right)^2\left(\frac{M_\bullet}{m}\right)^2\frac{1}{N}$$
$$\approx 0.23\left(\frac{C_{\rm SB}}{0.7}\right)^2\left(\frac{a}{\rm mpc}\right)^{-2}\left(\frac{M_\bullet}{10^6\mathcal{M}_\odot}\right)^4$$
$$\times\left(\frac{m}{10\mathcal{M}_\odot}\right)^{-2}\left(\frac{N}{10^2}\right)^{-1}; \quad (74)$$

here and below, N is the number of stars within radius a. $N(a) \propto a$ was not assumed in deriving this expression. However, that assumption *was* made in deriving Eq. (62), the condition that GW emission dominate stellar encounters. We can generalize that relation to a cluster with arbitrary density profile using the approximate scaling of the NR relaxation time:

$$t_{\rm NR} \propto \frac{M_\bullet^2}{m^2}\frac{P_r}{N} \tag{75}$$

[e.g. [16]], together with the exact, orbit-averaged expression for $t_{\rm NR}$ in the case $n(r) \propto r^{-2}$, Eq. (60), to write

$$t_{\rm NR} \approx 6\ {\rm Myr}\left(\frac{a}{\rm mpc}\right)^{3/2}\left(\frac{M_\bullet}{10^6\mathcal{M}_\odot}\right)^{3/2}\left(\frac{m}{10\mathcal{M}_\odot}\right)^{-2}\left(\frac{N}{10^2}\right)^{-1}. \tag{76}$$

The condition for GW emission to dominate relaxation then becomes

$$(1-e^2)_{\rm GW} \approx 2\times 10^{-3}\left(\frac{a}{\rm mpc}\right)^{-1}\left(\frac{M_\bullet}{10^6\mathcal{M}_\odot}\right)^{7/5} \times\left(\frac{m}{10\mathcal{M}_\odot}\right)^{-2/5}\left(\frac{N}{10^2}\right)^{-2/5}. \tag{77}$$

If physical capture by the MBH is assumed to occur when $r \le r_{\rm capt}$, $r_{\rm capt} = \Theta r_g$, then the critical eccentricity for capture is

$$(1-e^2)_{\rm capt} \approx 8\times 10^{-4}\left(\frac{\Theta}{8}\right)\left(\frac{a}{\rm mpc}\right)^{-1}\left(\frac{M_\bullet}{10^6\mathcal{M}_\odot}\right). \tag{78}$$

We define $a_{\rm plunge}$ to be the value of a such that $(1-e^2)_{\rm capt} = (1-e^2)_{\rm GW}$; at larger a, all stars plunge. We find that $a_{\rm plunge}$ is defined implicitly by

$$N(<a_{\rm plunge}) \approx 1.1\times 10^3\left(\frac{\Theta}{8}\right)^{-5/2}\left(\frac{M_\bullet}{10^6\mathcal{M}_\odot}\right)\left(\frac{m}{10\mathcal{M}_\odot}\right)^{-1}. \tag{79}$$

The Schwarzschild barrier intersects the GW line when

$$\left(\frac{a}{\rm mpc}\right)\left(\frac{N}{10^2}\right)^{3/5} \approx 120\left(\frac{C_{\rm SB}}{0.7}\right)^2\left(\frac{M_\bullet}{10^6\mathcal{M}_\odot}\right)^{13/5}\left(\frac{m}{10\mathcal{M}_\odot}\right)^{-8/5} \tag{80}$$

and it intersects the capture line when

$$\left(\frac{a}{\rm mpc}\right)\left(\frac{N}{10^2}\right) \approx 300\left(\frac{C_{\rm SB}}{0.7}\right)^2\left(\frac{\Theta}{8}\right)^{-1}\left(\frac{M_\bullet}{10^6\mathcal{M}_\odot}\right)^3\left(\frac{m}{10\mathcal{M}_\odot}\right)^{-2}. \tag{81}$$

One of these two relations defines the effective upper limit to the radial extent of the Schwarzschild barrier. Setting $e = 0$ in Eq. (74) gives the lower radial limit:

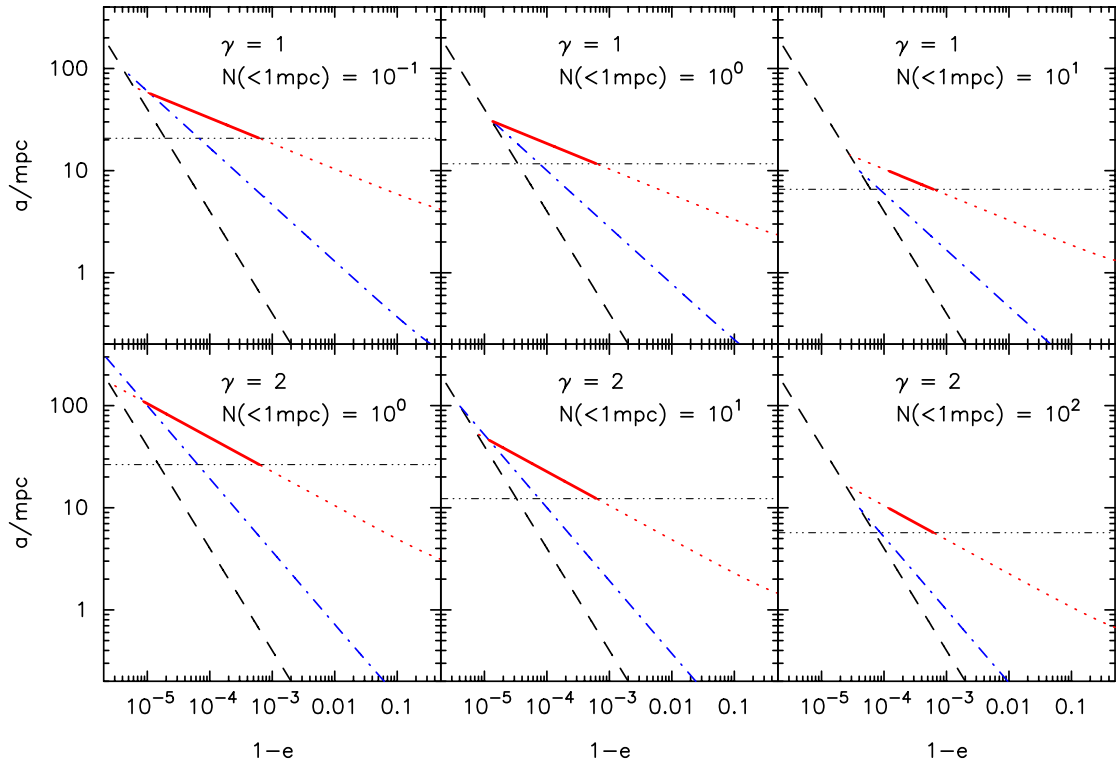

FIG. 14 (color online). Illustrating the critical curves defined in the text for nuclear star clusters obeying density laws $n(r) \propto r^{-\gamma}$, with various slopes and normalizations. *Dashed (black) line:* capture radius ($r_p = 8r_g$); *dash-dotted (blue) line:* radius at which GW emission dominates stellar perturbations, Eq. (77). The Schwarzschild barrier, Eq. (74), is shown as the red line; it is solid where conditions allow EMRI formation. Below the horizontal line, NRR is expected to be inefficient at pushing stars past the barrier (Eqs. (80), (81), and (83).) $M_\bullet = 10^6\mathcal{M}_\odot$ and $m = 10\mathcal{M}_\odot$ were assumed.

$$\left(\frac{a}{\mathrm{mpc}}\right)^2\left(\frac{N}{10^2}\right) \approx 0.2\left(\frac{C_{\mathrm{SB}}}{0.7}\right)^2\left(\frac{M_\bullet}{10^6\mathcal{M}_\odot}\right)^4\left(\frac{m}{10\mathcal{M}_\odot}\right)^{-2}. \tag{82}$$

Another key parameter is the minimum value of a for which NRR is able to penetrate the Schwarzschild barrier (Sec. V C). Combining Eqs. (51a), (66), (69), (50), and (74), we find that the critical value of a satisfies the implicit relation

$$\left(\frac{a}{\mathrm{mpc}}\right)_{\mathrm{penetrate}} \approx 15\left(\frac{C_{\mathrm{SB}}}{0.7}\right)\left(\frac{M_\bullet}{10^6\mathcal{M}_\odot}\right)^{5/2}\left(\frac{m}{10\mathcal{M}_\odot}\right)^{-3/2} \times\left(\frac{N}{10^2}\right)^{-1/2}. \tag{83}$$

In deriving this expression, we have equated t_{coh} with t_{M}.

We apply these expressions to nuclear star clusters obeying

$$n(r) = n_0 r^{-\gamma} \tag{84}$$

; i.e.

$$N \equiv N(<a) = N_{<1}\tilde{a}^{3-\gamma}, \tag{85}$$

where $\tilde{a} \equiv a/\mathrm{mpc}$ and $N_{<1}$ is the number of stars with $a \leq 1$ mpc. Combining Eqs. (85) and (83), we find

$$\tilde{a}_{\mathrm{penetrate}} \approx \left[140\left(\frac{C_{\mathrm{SB}}}{0.7}\right)\left(\frac{M_\bullet}{10^6\mathcal{M}_\odot}\right)^{5/2} \times\left(\frac{m}{10\mathcal{M}_\odot}\right)^{-3/2}N_{<1}^{-1/2}\right]^{2/(5-\gamma)}. \tag{86}$$

Figure 14 plots the relations defined above for clusters of $m = 10\mathcal{M}_\odot$ BHs around a $M_\bullet = 10^6\mathcal{M}_\odot$ MBH. We chose likely values of γ and $N_{<1}$ following the discussion in Ref. [19]. As in the N-body models, there is generally a rather small range of a values from which EMRIs can form: small enough that GW emission can overcome stellar perturbations, but large enough that NRR can push stars past the Schwarzschild barrier. Interestingly, for sufficiently dense clusters, this range can go to zero, implying essentially no EMRIs; however, it appears that the required densities are one or two orders of magnitude larger than expected for real galactic nuclei [19].

VII. CONCLUSIONS

(1) N-body integrations have been used, for the first time, to directly simulate the long-term evolution of relativistic clusters of compact stars around MBHs, both Schwarzschild and Kerr, and to compute the rate of EMRIs.
(2) When relativistic terms are omitted from the equations of motion, stars are scattered into the MBH at rates that are in good agreement with those expected from the theory of RR..
(3) Relativistic precession suppresses RR, leading to an effectively maximum value of the eccentricity at each value of the semi-major axis. This "Schwarzschild barrier" strongly inhibits EMRI formation, leading to capture rates that are factors ~10–100 lower than in the non-relativistic case.
(4) We use an approximate Hamiltonian formulation of the perturbed equations of motion to explore two possible mechanisms for barrier penetration: one related to RR and the other to NRR. We show that NR is effective at penetrating the Schwarzschild barrier only for orbits with semi-major axes above a certain value, and this prediction is verified in the N-body integrations. Approximate expressions for the capture rate are derived and shown to be consistent with the rates observed in the simulations.

ACKNOWLEDGMENTS

D. M. was supported in part by the National Science Foundation under Grants No. AST 08-07910 and 08-21141, and by the National Aeronautics and Space Administration under Grant No. NNX-07AH15G. T. A. was supported by ERC Starting Grant No. 202996, and by DIP-BMBF Grant No. 71-0460-0101. C. M. W. was supported in part by the National Science Foundation under Grants No. PHY 06-52448 and 0965133, the National Aeronautics and Space Administration Grant No. NNG- 06GI60G, and the Centre National de la Recherche Scientifique, Programme Internationale de la Coopération Scientifique (CNRS-PICS) Grant No. 4396. Parts of this research were carried out while C. M. W. was a visitor to the Institut d'Astrophysique de Paris, and while D. M., S. M. and C. M. W. were visitors to the Benoziyo Center for Astrophysics, Weizmann Institute of Science; the hospitality of these two institutes is gratefully acknowledged. We thank P. Amaro-Seoane, B. Baror, and P. Saha for useful discussions.

APPENDIX A: HAMILTONIAN MODEL

Here we use standard techniques [e.g. [27]] to derive the equations describing the rates of change of the Keplerian (osculating) elements of a star moving in the potential (37):

$$\Phi(\mathbf{r}) = -\frac{GM_\bullet}{r} + \Phi_p,\ \Phi_p = \Phi_s \ln\left(\frac{r}{r_o}\right) - Sa\cos\theta \tag{A1}$$

and including the time-averaged effects of Schwarzschild precession.

We begin by transforming from Cartesian coordinates to Delaunay variables [e.g. [41]] which are action-angle variables in the Kepler problem. The Delaunay action variables are the radial action $I = (GM_\bullet a)^{1/2}$, the angular momentum L, and the projection of $\mathbf{L}$ onto the z axis L_z. The conjugate angle variables are the mean anomaly w, the

argument of the periapse ω, and the longitude of the ascending node Ω. In the Keplerian case, five of these are constants; the exception is w which increases linearly with time at a rate

$$\nu_r = (GM_\bullet)^2/I^3. \tag{A2}$$

The Hamiltonian, averaged over w, is

$$\bar{\mathcal{H}} = -\frac{1}{2}\left(\frac{GM_\bullet}{I}\right)^2 + \bar{\Phi}_p, \tag{A3a}$$

$$\bar{\Phi}_p \equiv \oint \frac{dw}{2\pi}\Phi_p = \frac{1}{2\pi}\int_0^{2\pi} dE(1 - e\cos E)\Phi_p(\mathbf{r}). \tag{A3b}$$

In the final term, E is the eccentric anomaly, where $r = a(1 - e\cos E)$ and the eccentricity is $e = \sqrt{1 - L^2/I^2}$. After the averaging, $\bar{\mathcal{H}}$ is independent of w, and I is conserved, as is the semi-major axis a. We are left with four variables and with $\bar{\Phi}_p$ as the effective Hamiltonian of the system.

The orbit-averaged Hamiltonian describes slow, precessional dynamics. Superposed on the slow variations described by the averaged dynamics are fast oscillations, with frequencies $\sim(GM_\bullet/a^3)^{1/2}$ and with fractional amplitudes $\delta \approx a(\Phi - \bar{\Phi})/GM_\bullet$. If $\delta \ll 1$, i.e. if $M_\bullet \gg M_\star$, we can ignore these fast oscillations.

After expressing the Cartesian coordinates in terms of the Delaunay variables, the results of the averaging are

$$\bar{\Phi}_p = \bar{\Phi}_M + \bar{\Phi}_D + \bar{\Phi}_{\rm GR}, \tag{A4a}$$

$$\bar{\Phi}_M = \frac{GM(a)}{a}[C(a) + F(e)], \tag{A4b}$$

$$C(a) = \ln\left(\frac{a}{r_0}\right) + 1 - \ln 2,$$

$$F(e) = \ln(1 + \sqrt{1 - e^2}) - \sqrt{1 - e^2}, \tag{A4c}$$

$$\bar{\Phi}_D = Sae\sin i\sin\omega, \tag{A4d}$$

$$\bar{\Phi}_{\rm GR} = -\frac{3G^2M_\bullet^2}{c^2a^2}(1 - e^2)^{-1/2}. \tag{A4e}$$

The averaged dipole potential, $\bar{\Phi}_D$, is expressed in terms of the orbital inclination i, where $\cos i = L_z/L$; $i = 0$ for an orbit that is perpendicular to the major axis of the dipole. The last term, $\bar{\Phi}_{\rm GR}$, reproduces the orbit-averaged rate of Schwarzschild periapse advance, Eq. (16). The longitude of the ascending node, Ω, does not appear due to symmetry of the potential about the z-axis.

In the limit $e \to 1$, $F(e) \to -\ell^2/2$.

We define a dimensionless time $\tau = \nu_0 t$, where

$$\nu_0 = \nu_r\frac{3GM_\bullet}{c^2a}, \tag{A5}$$

the Schwarzschild precession frequency in the limit $e \to 0$. Dropping constant terms (including terms that depend only on semi-major axis a), the dimensionless Hamiltonian describing the perturbed motion becomes

$$H \equiv \frac{\bar{\Phi}_p}{\nu_0 I} = -(1 - e^2)^{-1/2} + A_M F(e) + A_D e\sin i\sin\omega, \tag{A6}$$

with $A_{\rm M}$, A_D defined in Eq. (43). The equations of motion,

$$\begin{aligned} \frac{\partial\omega}{\partial\tau} &= \frac{\partial H}{\partial\ell}, & \frac{\partial\ell}{\partial\tau} &= -\frac{\partial H}{\partial\omega}, \\ \frac{\partial\Omega}{\partial\tau} &= \frac{\partial H}{\partial\ell_z}, & \frac{\partial\ell_z}{\partial\tau} &= -\frac{\partial H}{\partial\Omega} = 0 \end{aligned} \tag{A7}$$

are given explicitly in Eqs. (41).

APPENDIX B: NON-RESONANT RELAXATION

Here we summarize the orbit-averaged equations describing changes in angular momentum due to NRR and derive the angular-momentum diffusion coefficient for the N-body models [e.g. [32,42,43]].

In terms of the binding energy per unit mass $E = -v^2/2 + \psi(r) = GM_\bullet/2a$, where $\psi(r) = GM_\bullet/r$, and the normalized angular momentum $R \equiv L^2/L_c^2 = \ell^2 = 1 - e^2$, the Fokker-Planck equation describing diffusion in angular momentum due to NR is

$$\frac{\partial N}{\partial t} = \frac{1}{2}\frac{\partial}{\partial R}\left[\langle(\Delta R)^2\rangle\frac{\partial N}{\partial R}\right], \tag{B1}$$

where

$$N(E, R)dEdR = N(a, e)dade \tag{B2}$$

is the number density of stars in (energy, angular momentum) space, and $\langle(\Delta R)^2\rangle$ is the diffusion coefficient in R; i.e. the sum, over a unit interval of time, of $(\Delta R)^2$ due to encounters.

Taking the limit $R \to 0$ and averaging over one orbital period, this becomes

$$\frac{\partial N}{\partial t} = \bar{\mu}\frac{\partial}{\partial R}\left(R\frac{\partial N}{\partial R}\right), \tag{B3}$$

where $\bar{\mu}(E)$ is the orbit-averaged diffusion coefficient:

$$\bar{\mu}(E) \equiv P_r(E)^{-1}\oint\frac{dr}{v_r}\lim_{R\to 0}\frac{\langle(\Delta R)^2\rangle}{2R} \tag{B4}$$

and the integral is over one full radial period. $\bar{\mu}(E)$ is precisely the orbit average of the inverse angular momentum relaxation time defined by Hopman & Alexander [44] and henceforth we write $\bar{\mu}^{-1} \equiv t_{\rm NR}$.

Let $f(E)$ be the phase-space number density of stars; it is related to $N(E)$ by

$$f(E) = \frac{1}{\sqrt{2}\pi^3}(GM_\bullet)^{-3}E^{5/2}N(E) \tag{B5}$$

$$= f_0E^{\gamma-3/2}. \tag{B6}$$

The latter expression assumes $n(r) \propto r^{-\gamma}$; the N-body models have $\gamma = 2$. The local diffusion coefficient is expressible in terms of $f(E)$ via

$$\lim_{R\to 0}\frac{\langle(\Delta R)^2\rangle}{2R} = \frac{32\pi^2 r^2 G^2 m^2 \ln\Lambda}{3L_c^2} \times (3I_{1/2} - I_{3/2} + 2I_0), \tag{B7a}$$

$$I_0(E) = \int_0^E f(E')dE', \tag{B7b}$$

$$I_{n/2}(E, r) = \{2[\psi(r) - E]\}^{-n/2} \times \int_E^\psi \{2[\psi(r) - E']\}^{n/2} f(E')dE', \tag{B7c}$$

where $\ln\Lambda \approx \ln[M_\bullet/(2m)]$ is the Coulomb logarithm; in the N-body models $\ln\Lambda \approx 9$.

The orbit averages are

$$\bar{I}(E) = \frac{1}{\sqrt{2}}\int_0^{GM_\bullet/E} \frac{r^2 dr}{\sqrt{\Psi - E}} I(E, r); \tag{B8}$$

setting $\gamma = 2$, the value in the N-body models, we find

$$\bar{I}_0(E) = \frac{5\sqrt{2}\pi}{48} f_0 E^{-2}(GM_\bullet)^3, \tag{B9a}$$

$$\bar{I}_{1/2}(E) = \frac{\pi}{16\sqrt{2}}(\ln 16 - 2) f_0 E^{-2}(GM_\bullet)^3, \tag{B9b}$$

$$\bar{I}_{3/2}(E) = \frac{\pi}{96\sqrt{2}}(11 - 12\ln 2) f_0 E^{-2}(GM_\bullet)^3 \tag{B9c}$$

and

$$3\bar{I}_{1/2} - \bar{I}_{3/2} + 2\bar{I}_0 = C_\gamma f_0 E^{-2}(GM_\bullet)^3, \tag{B10a}$$

$$C_2 = \frac{7\pi\sqrt{2}}{192}(12\ln 2 - 1) \tag{B10b}$$

$$\approx 1\,18533\,; \tag{B10c}$$

so that

$$\bar{\mu}(E) = C_2 \frac{64\pi\sqrt{2}}{3} G^2 m^2 \ln\Lambda f(E). \tag{B11}$$

We note that $\bar{\mu}(E) \propto f(E)$, a result that holds for arbitrary γ.

Equations (2), (B2), and (B5) combine to give f in terms of a:

$$f(a) = \frac{1}{4\pi^3}(GM_\bullet)^{-3/2} N_0 a^{-1/2}; \tag{B12}$$

where $N_0 = r^{-1}N(<r) = a^{-1}N(<a)$. Then

$$\bar{\mu}^{-1}(a) \equiv t_{\rm NR}(a) = C_2^{-1}\frac{3\sqrt{2}\pi^2}{32}\frac{(GM_\bullet)^{3/2}}{G^2 m^2 N_0 \ln\Lambda} a^{1/2}. \tag{B13}$$

[1] K. Danzmann , Classical Quantum Gravity**14**, 1399 (1997).
[2] S. A. Hughes, Ann. Phys. (N.Y.) **303**, 142 (2003).
[3] L. Barack and C. Cutler, Phys. Rev. D **69**, 082005 (2004).
[4] P. Amaro-Seoane, J. R. Gair, M. Freitag, M. C. Miller, I. Mandel, C. J. Cutler, and S. Babak, Classical Quantum Gravity **24**, R113 (2007).
[5] Capture onto more nearly circular orbits could occur if the compact object was originally a member of a bound pair; see Miller *et al.*, Astrophys. J. Lett. **631**, L117 (2005).
[6] J. R. Gair, L. Barack, T. Creighton, C. Cutler, S. L. Larson, E. S. Phinney, and M. Vallisneri, Classical Quantum Gravity **21**, S1595 (2004).
[7] L. Wen and J. R. Gair, Classical Quantum Gravity **22**, S445 (2005).
[8] N. J. Cornish and J. Crowder, Phys. Rev. D **72**, 043005 (2005).
[9] F. D. Ryan, Phys. Rev. D **52**, 5707 (1995).
[10] E. Berti, A. Buonanno, and C. M. Will, Classical Quantum Gravity **22**, S943 (2005).
[11] S. Drasco, Classical Quantum Gravity **23**, S769 (2006).
[12] D. Hils and P. L. Bender, Astrophys. J. Lett. **445**, L7 (1995).
[13] S. Sigurdsson and M. J. Rees, Mon. Not. R. Astron. Soc. **284**, 318 (1997).
[14] P. B. Ivanov, Mon. Not. R. Astron. Soc. **336**, 373 (2002).
[15] C. Hopman and T. Alexander, Astrophys. J. Lett. **645**, L133 (2006).
[16] C. Hopman and T. Alexander, Astrophys. J. **645**, 1152 (2006).
[17] M. Freitag, P. Amaro-Seoane, and V. Kalogera, Astrophys. J. **649**, 91 (2006).
[18] D. Merritt, Astrophys. J. **718**, 739 (2010).
[19] D. Merritt, T. Alexander, S. Mikkola, and C. M. Will, Phys. Rev. D **81**, 062002 (2010).
[20] K. P. Rauch and S. Tremaine, New Astron **1**, 149 (1996).
[21] S. E. Woosley, A. Heger, and T. A. Weaver, Rev. Mod. Phys. **74**, 1015 (2002).
[22] J. N. Bahcall and R. A. Wolf, Astrophys. J. **216**, 883 (1977).
[23] T. Alexander and C. Hopman, Astrophys. J. **697**, 1861 (2009).
[24] S. Mikkola and D. Merritt, Mon. Not. R. Astron. Soc. **372**, 219 (2006).
[25] S. Mikkola and D. Merritt, Astron. J. **135**, 2398 (2008).
[26] C. Cutler, D. Kennefick, and E. Poisson, Phys. Rev. D **50**, 3816 (1994).

[27] D. Merritt and E. Vasiliev, Astrophys. J. **726**, 61 (2011).
[28] Throughout this paper we use P to denote a full period of oscillation or libration, while $t_X \equiv \pi/\nu_x$ is the time for angular variable X to change by π.
[29] M. A. Gürkan and C. Hopman, Mon. Not. R. Astron. Soc. **379**, 1083 (2007).
[30] E. Eilon, G. Kupi, and T. Alexander, Astrophys. J. **698**, 641 (2009).
[31] H. Cohn and R. M. Kulsrud, Astrophys. J. **226**, 1087 (1978).
[32] A. P. Lightman and S. L. Shapiro, Astrophys. J. **211**, 244 (1977).
[33] P. C. Peters, Phys. Rev. **136**, B1224 (1964).
[34] T. Damour and N. Deruelle, Ann. I.H.P. Phys. Théor. **43**, 107 (1985).
[35] So-called to distinguish it from precession associated with frame-dragging, or Kerr precession, in which the line of nodes changes. Other names for precession induced by the Schwarzschild part of the metric include geodetic and de Sitter precession.
[36] L. D. Landau and E. M. Lifshitz, *Mechanics* (Pergamon, New York, 1976).
[37] M. Belyaev and R. Rafikov, Astrophys. J. **723**, 1718 (2010).
[38] T. Alexander and D. Merritt (unpublished).
[39] T. Isobe, Ph.D. thesis, Pennsylvania State University, 1989.
[40] T. Alexander, B. Baror, and D. Merritt (unpublished).
[41] H. Goldstein, C. Poole, and J. Safko, *Classical Mechanics* (Addison-Wesley, San Francisco, 2002).
[42] J. Magorrian and S. Tremaine, Mon. Not. R. Astron. Soc. **309**, 447 (1999).
[43] M. Milosavljević and D. Merritt, Astrophys. J. **596**, 860 (2003).
[44] C. Hopman and T. Alexander, Astrophys. J. **629**, 362 (2005).